

Expanding the High- z Supernova Frontier: “Wide-Area” JWST Discoveries from the First Two Years of COSMOS-Web

ORI D. FOX,¹ ARMIN REST,^{1,2} JUSTIN D. R. PIEREL,¹ DAVID A. COULTER,¹ CAITLIN M. CASEY,^{3,4}
 JEYHAN S. KARTALTEPE,⁵ HOLLIS B. AKINS,^{6,*} MAXIMILIEN FRANCO,⁷ MIKE ENGESER,¹ CONOR LARISON,¹
 TAKASHI J. MORIYA,^{8,9,10} ROBERT M. QUIMBY,^{11,12} MARKO SHUNTOV,^{4,13,14} MATTHEW R. SIEBERT,¹
 CHRISTA DECOURSEY,¹⁵ JAMES M. DERKACY,¹ NICOLE E. DRAKOS,¹⁶ EIICHI EGAMI,¹⁵ STEVEN L. FINKELSTEIN,^{6,17}
 CARTER FLAYHART,⁵ SEIJI FUJIMOTO,^{18,19} ESTEFANIA PADILLA GONZALEZ,¹ MASSIMO GRIGGIO,¹ SANTOSH HARISH,^{1,5}
 OLIVIER ILBERT,²⁰ KOHEI INAYOSHI,^{21,†} ANTON M. KOEKEMOER,¹ VASILY KOKOREV,⁶ CLOTILDE LAIGLE,²²
 ERINI LAMBRIDES,²³ REBECCA L. LARSON,¹ DAIZHONG LIU,²⁴ GEORGIOS E. MAGDIS,^{4,25} JACQUELINE E. MCCLEARY,²⁶
 HENRY J. MCCRACKEN,²² NICOLAS MCMAHON,⁵ JED MCKINNEY,^{6,‡} THOMAS MOORE,¹ LOUISE PAQUEREAU,²²
 JASON RHODES,²⁷ BRANT E. ROBERTSON,²⁸ DAVID B. SANDERS,²⁹ SOGOL SANJARIPOUR,³⁰ KOJI SHUKAWA,²
 LOUIS-GREGORY STROLGER,¹ SUNE TOFT,^{29,4,13} QINAN WANG,³¹ ROBERT E. WILLIAMS,¹ AND YOSSEF ZENATI^{2,32,33}

¹Space Telescope Science Institute, 3700 San Martin Drive, Baltimore, MD 21218, USA

²William H. Miller III Department of Physics & Astronomy, Johns Hopkins University, 3701 San Martin Dr, Baltimore, MD 21218, USA

³Department of Physics, University of California, Santa Barbara, Santa Barbara, CA 93106, USA

⁴Cosmic Dawn Center (DAWN), Jagtvej 128, DK2200 Copenhagen N, Denmark

⁵Laboratory for Multiwavelength Astrophysics, School of Physics and Astronomy, Rochester Institute of Technology, 84 Lomb Memorial Drive, Rochester, NY 14623, USA

⁶Department of Astronomy, The University of Texas at Austin, 2515 Speedway Blvd Stop C1400, Austin, TX 78712, USA

⁷Université Paris-Saclay, Université Paris Cité, CEA, CNRS, AIM, 91191 Gif-sur-Yvette, France

⁸National Astronomical Observatory of Japan, National Institutes of Natural Sciences, 2-21-1 Osawa, Mitaka, Tokyo 181-8588, Japan

⁹Graduate Institute for Advanced Studies, SOKENDAI, 2-21-1 Osawa, Mitaka, Tokyo 181-8588, Japan

¹⁰School of Physics and Astronomy, Monash University, Clayton, VIC 3800, Australia

¹¹Department of Astronomy and Mount Laguna Observatory,

San Diego State University, San Diego, CA 92182, USA

¹²Kavli Institute for the Physics and Mathematics of the Universe (WPI), The University of Tokyo Institutes for Advanced Study, The University of Tokyo, Kashiwa, Chiba 277-8583, Japan

¹³Niels Bohr Institute, University of Copenhagen, Jagtvej 128, DK-2200, Copenhagen, Denmark

¹⁴University of Geneva, 24 rue du Général-Dufour, 1211 Genève 4, Switzerland

¹⁵Steward Observatory, University of Arizona, 933 N. Cherry Ave, Tucson, AZ 85721, USA

¹⁶Department of Physics and Astronomy, University of Hawaii, Hilo, 200 W Kawili St, Hilo, HI 96720, USA

¹⁷Cosmic Frontier Center, The University of Texas at Austin, Austin, TX, USA

¹⁸David A. Dunlap Department of Astronomy and Astrophysics, University of Toronto, 50 St. George Street, Toronto, Ontario, M5S 3H4, Canada

¹⁹Dunlap Institute for Astronomy and Astrophysics, 50 St. George Street, Toronto, Ontario, M5S 3H4, Canada

²⁰Aix Marseille Univ, CNRS, CNES, LAM, Marseille, France

²¹Kavli Institute for Astronomy and Astrophysics, Peking University, Beijing 100871, China

²²Institut d’Astrophysique de Paris, UMR 7095, CNRS, and Sorbonne Université, 98bis boulevard Arago, 75014 Paris, France

²³NASA-Goddard Space Flight Center, Greenbelt MD, 20771, USA

²⁴Purple Mountain Observatory, Chinese Academy of Sciences, 10 Yuanhua Road, Nanjing 210023, China

²⁵DTU-Space, Technical University of Denmark, Elektrovej 327, 2800, Kgs. Lyngby, Denmark

²⁶Department of Physics, Northeastern University, 360 Huntington Ave, Boston, MA

²⁷Jet Propulsion Laboratory, California Institute of Technology, 4800 Oak Grove Drive, Pasadena, CA 91001, USA

²⁸Department of Astronomy and Astrophysics, University of California, Santa Cruz, 1156 High Street, Santa Cruz, CA 95064, USA

²⁹Institute for Astronomy, University of Hawai’i at Manoa, 2680 Woodlawn Drive, Honolulu, HI 96822, USA

³⁰Department of Physics and Astronomy, University of California Riverside, Riverside, CA 92521, USA

³¹Department of Physics and Kavli Institute for Astrophysics and Space Research, Massachusetts Institute of Technology, 77 Massachusetts Avenue, Cambridge, MA 02139, USA

³²Astrophysics Research Center of The Open University (ARCO), Ra'anana 4353701, Israel

³³Department of Natural Sciences, The Open University of Israel, Ra'anana 4353701, Israel

ABSTRACT

Transient astronomy in the early Universe ($z \gtrsim 2$) remains largely unexplored, lying beyond the rest-frame optical spectroscopic reach of most current observatories. Yet this regime promises transformative insights, with high-redshift transients providing direct access to the early Universe and enabling studies of how stellar populations and cosmology evolve over cosmic time. JWST is uniquely equipped to probe these redshifts efficiently in the rest-frame optical and near-IR. We present results from an initial pathfinder search, covering an area of ~ 133 arcmin 2 (~ 0.037 deg 2) independently imaged by the PRIMER and COSMOS-Web (hereafter COSMOS) extragalactic surveys. Although neither program was designed for time-domain astronomy, combining their data results in difference images separated by roughly one year, leading to the discovery of 68 supernovae (SNe) with host photometric redshifts reaching $z \lesssim 5$. For most SNe, only a single epoch is available, but the combination of host redshift, classification, color, and magnitude enables us to prioritize candidates for detailed photometric and spectroscopic follow-up. Among the most notable sources are a relatively bright, blue CCSN at $z > 3$ (SN 2023aeab) and a young, normal SN Ia at $z > 2$ (SN 2023aeax). The sample distribution highlights the increasing likelihood that a wide-area JWST program can uncover younger, bluer, and potentially more extreme explosions. While this pathfinder effort is limited in cadence and number of filters, it demonstrates the strong potential of a dedicated, well-planned time-domain survey with JWST to obtain the sample sizes and rate measurements needed to chart SN populations deep into the early Universe.

Keywords: Supernovae (1668) – Core-collapse supernovae (304) – Type Ia supernovae (1728) – High-redshift galaxies (734) – High-redshift supernovae (2037) – Transient detection (1957) – Time-domain astronomy (2109) – Surveys (1671) – Deep field astronomy (2216) – Cosmic reionization (1889) – Early Universe (435) – Galaxy photometry (611) – Photometric redshift (1273) – James Webb Space Telescope (2291)

1. INTRODUCTION

Given their large intrinsic luminosities, supernovae (SNe) offer a powerful alternative to stars as probes of the earlier Universe ($z > 1$). These explosions not only enable us to extend current low- z SN investigations to unique redshift ranges and host environments, but they also introduce new opportunities to study the first stars and the most formative years in the evolution of the Universe, including the peak era of star formation and black hole growth in the Universe’s history (i.e., Cosmic Noon) and the Epoch of Reionization (EoR). In particular, a statistically significant sample of high- z SNe can uniquely extend SN Ia cosmology to $z > 3$ (e.g., [J. D. R. Pierel et al., 2024, 2025](#)), enable the discovery and characterization of superluminous (SLSNe) and pair-instability SNe (PISNe) from low-metallicity and/or Pop III stars (e.g., [J. Jeon et al., 2026; A. Ferrara et al., 2026](#)), and track the evolution of Type II/Ib/Ic core-collapse SN (CCSN) explosions and their rates prior Cosmic Noon (e.g., [C. DeCoursey et al.,](#)

[2025a](#)). The evolution of the CCSN rates provides an independent test of the evolution of the cosmic star formation rate density (SFRD), independent of conversions from luminosity to SFR and dust corrections.

Yet transient astronomy at higher redshifts has remained relatively unexplored, given limitations in sensitivity and wavelength ranges of most current ground-based discovery surveys and follow-up facilities. Over the past decade, there has been an increasing effort to discover and follow up high- z SNe. Several ground-based studies have successfully detected a handful of superluminous supernovae (SLSNe) and bright SNe IIn at $2 < z < 3$ in deep stack survey data (e.g., [J. Cooke et al., 2009, 2012; M. Smith et al., 2018; C. Curtin et al., 2019; T. J. Moriya et al., 2019; A. Gal-Yam, 2019](#)). These discoveries have set the stage for larger space-based telescopes, such as the *James Webb Space Telescope* (JWST) and the *Nancy Grace Roman Space Telescope* (hereafter *Roman*).

Compared to ground-based telescopes, the distinct sensitivity and wavelength coverage of JWST enables not only detection of high-redshift SNe, but both high signal-to-noise photometric and spectroscopic monitoring throughout most of their evolution during the free-expansion phase. The combination of high angular res-

* NSF Graduate Research Fellow

†

‡ NASA Hubble Fellow

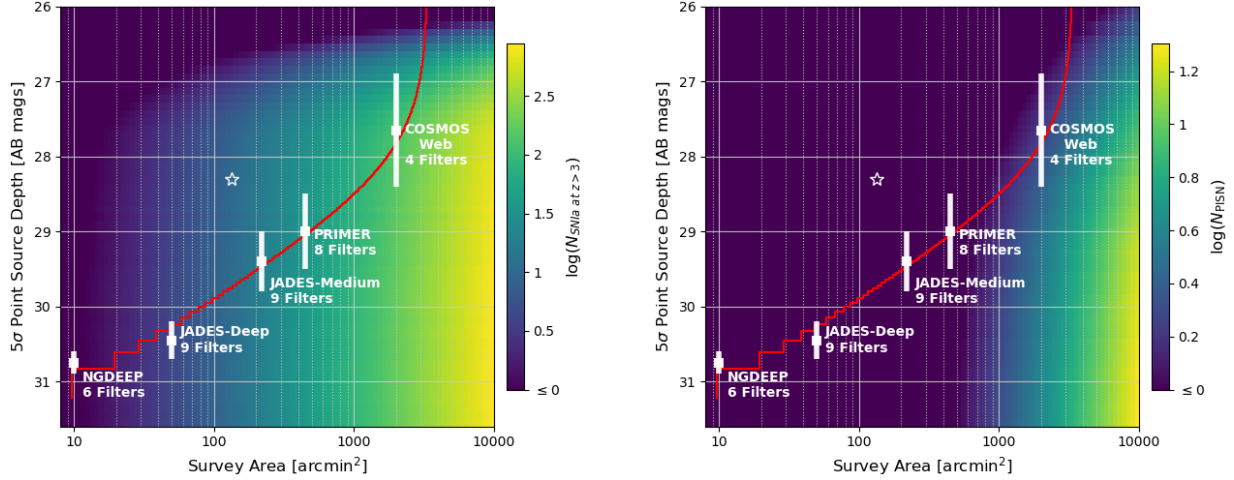


Figure 1. Total expected number of SNe derived from simulations of a corresponding 5-year survey: (left) Type Ia SNe at redshifts $z > 3$; (right) Pop-III PISNe. For simplicity, the simulated surveys all have a 6-month cadence in four JWST/NIRcam bands (F115W, F150W, F277W, and F444W), all with the same limiting magnitude per epoch. The SN yields correspond to the number of SNe detected in at least one band at any phase. The red line traces the area and magnitude limits possible with 200 hours on JWST (including overheads). Increasing depth has limited benefits below about 28th magnitude, but the survey yields increase proportionally with survey area. The area and depths of several Cycle 1 JWST surveys are marked for comparison, but note these surveys are not uniform and all have different durations, filters, and cadences from the simulations. The open star marks the overlapping area of COSMOS-Web and PRIMER used in this paper (see Figure 2).

olution with stable, low-background imaging facilitates effective host-galaxy subtraction and allows for concurrent characterization of SN environments, including stellar mass, star formation rate (SFR), and metallicity. These measurements are challenging to acquire from ground-based observations at comparable redshifts.

Despite JWST’s advantages, SN discoveries to date have been relatively sparse. Some of the earliest successes came from targeting lensing clusters (i.e., H. Yan et al., 2023; W. Chen et al., 2024), but these early discoveries had no JWST templates and instead required *Hubble Space Telescope* (HST) templates for their subtraction. HST templates are not only shallower, but most SN emission redshifts out of HST’s filters at $z \gtrsim 3$, limiting all early lensing discoveries to $z \lesssim 3$. Building the necessary statistically significant, well-characterized sample requires a survey that is both wide and deep with sufficient follow-up opportunities (S. W. Jha et al., 2024). Such surveys require significant observational time, even with JWST’s exquisite sensitivity, because of the telescope’s narrow field of view and large overheads. Consequently, these time-domain science observing programs have faced difficulty securing approval. As a result, the time-domain community is increasingly leveraging the existing, serendipitous fields obtained for other science programs (Figure 1). Section 6.2 provides a more detailed discussion on the tradeoffs between depth and area.

One of the highest-yield discovery programs to date has been the JWST Advanced Deep Extragalactic Sur-

vey (JADES; D. J. Eisenstein et al., 2023), which obtained deep, multi-epoch imaging with a primary science goal of exploring high-redshift galaxies. The survey obtained two sets of deep NIRCam images covering an area of ~ 25 arcmin 2 over the GOODS-S field with a separation of 1 year, which has enabled a transient survey of unprecedented depth (down to ~ 30 AB mag). From these observations, C. DeCoursey et al. (2025a) identified 79 transients (i.e., > 1 transient/arcmin 2 per epoch) with host redshifts ranging from $0.2 < z \lesssim 5$ (C. DeCoursey et al., 2025b). A follow-up DD proposal (PID 6541; PI Egami) observed eleven SNe with a single pointing of a NIRSpec/MSA spectroscopy and NIRCam imaging. The results of that spectroscopic program include an broad-lined Type Ic SN (Ic-BL) at $z=2.83$, which indicates this subclass may be more common at high z (M. R. Siebert et al., 2024), an SN Ia at $z=2.9$ that tests an evolving dark energy in a dark-matter dominated Universe (J. D. R. Pierel et al., 2024), and a UV-bright SN at $z=3.6$ (D. A. Coulter et al., 2025). The follow-up spectroscopy and imaging also realized the first systematic characterization of high-redshift SNe II (T. J. Moriya et al., 2025).

While JADES successfully discovered dozens of new SNe, its survey footprint was relatively narrow (~ 25 arcmin 2). A much larger area is covered by the overlap of JWST Cosmic Evolution Survey (COSMOS-Web; PID 1727) and the Public Release IMaging for Extragalactic Research (PRIMER; PID 1837) Surveys (see Section 2). These two Cycle 1 Treasury Programs,

when taken together, obtained overlapping images in 4 NIRCam filters (F115W, F150W, F277W, F444W) in an area that is > 5 times larger than JADES (133 arcmin 2), but not as deep (~ 28 mag on average). This field also benefits from the fact that the COSMOS data products include extensive photometric and spectroscopic redshift catalogs.

In this article we present transient discoveries from the overlap of the COSMOS-Web and PRIMER data sets. Section 2 presents the observations and reduction techniques. Section 3 outlines the transient/SNe identification criteria, explains how photometry was performed, and provides an analysis of the discovery epoch detection limit. Section 4 presents an analysis of the data, including host galaxy redshifts, single-epoch photometric SN classification, and evaluation of the various SN parameters. Section 5 describes candidate prioritization, identification, and follow-up photometry and spectroscopy. Section 6 provides a discussion of the results, considerations and requirements for an optimal transient survey with JWST, and synergies with *Roman*. Finally, in Section 7, we summarize the paper and highlight the primary takeaways. Throughout this paper, we use magnitudes in the AB system (J. B. Oke & J. E. Gunn, 1983) and adopt the standard λ CDM cosmological parameters: $H_0 = 70 \text{ km s}^{-1} \text{ Mpc}^{-3}$, $\Omega_{\text{tot}} = 1.0$, $\Omega_{\Lambda} = 0.7$, and $\Omega_m = 0.3$.

2. OBSERVATIONS

2.1. COSMOS-Web

COSMOS is a well-known deep, wide area, multi-wavelength survey aimed at measuring the evolution of galaxies on scales from a few kpc to tens of Mpc (N. Scoville et al., 2007), centered at (J2000): 10:00:28.600 +02:12:21.00. COSMOS-Web (Program ID 1727; C. M. Casey et al., 2023) is a 255 hour wide-field Cycle 1 JWST treasury program that maps a contiguous $\sim 0.54 \text{ deg}^2$ (2000 arcmin 2) area in the center of the COSMOS field that has revolutionized our understanding of reionization’s spatial distribution, environments, and drivers at early stages by detecting thousands of galaxies in the EoR ($6 < z < 11$) on scales large enough to mitigate cosmic variance (e.g., C. M. Casey et al., 2024; H. B. Akins et al., 2025). The mosaiced observations were obtained with NIRCam in four filters: F115W, F150W, F277W, and F444W. Observations were split over four epochs for scheduling purposes: January 2023, April 2023, January 2024, and April 2024. The individual pointings had little to no overlap between the different epochs, although the fourth epoch was primarily focused on previously failed visits. The majority of the mosaic either has an on-sky exposure time of 513 s or 1030 s and reaches a

depth of roughly 27-28 AB mag. Additional details regarding the observations and reductions are outlined in the COSMOS-Web overview paper (C. M. Casey et al., 2024).

2.2. PRIMER

PRIMER (Public Release IMaging for Extragalactic Research) is another Cycle 1 Program (Program ID 1837 J. S. Dunlop et al., 2021) designed to provide deep, large-area, homogeneous JWST NIRCam+MIRI imaging survey of the COSMOS and UKIDSS Ultra-Deep Field (UDS). The PRIMER-COSMOS observations only cover $\sim 0.037 \text{ deg}^2$ ($\sim 133 \text{ arcmin}^2$) of the COSMOS field, but reach a depth of roughly 28-29 AB mag. The mosaiced observations were obtained with NIRCam in ten filters (F090W, F115W, F150W, F200W, F277W, F356W, F444W and F410M) and with MIRI in two filters (F770W and F1800W). Observations were split over three epochs for scheduling purposes: December 2022, April 2023, and December 2023. Again, the individual pointings had little to no overlap between epochs except the last epoch that re-observed failed visits. Additional details regarding the observations and reductions are outlined in the PRIMER overview paper (J. S. Dunlop et al., 2021).

Given the overlap of the two surveys and the difference in time of the observations, a number of pointings have two (and sometimes more in rare cases with serendipitous observations from other programs) epochs of observations spaced roughly a year apart. These two epochs offer an ideal pathfinder for a wide-field, relatively deep survey for discovery of transients with JWST in the second epoch, although no dedicated follow-up photometric or spectroscopic observations were available. The overlap between COSMOS and PRIMER is shown in Figure 2 (see also Figure 15 of C. M. Casey et al. 2024).

3. CANDIDATE DISCOVERY

Transient discovery traditionally requires difference imaging by template subtraction (see Section 3.2 and 3.3). Although this is a well-understood technique for many ground-based telescopes where the PSF is dominated by the “seeing” and can be modeled by Gaussian-like functions, space-based telescopes present a whole new level of complication (i.e., non-Gaussian PSF, field rotation, and alignment; E. M. Berman et al., 2024). Furthermore, given the resolution of JWST, optimal differencing requires precise alignment down to sub-pixels (i.e., ~ 0.1 pixels), but is typically only good to within ~ 1 pixel using the default pipeline (H. Bushouse et al., 2023; C. DeCoursey et al., 2025a; J. D. R. Pierel et al., 2025). To make

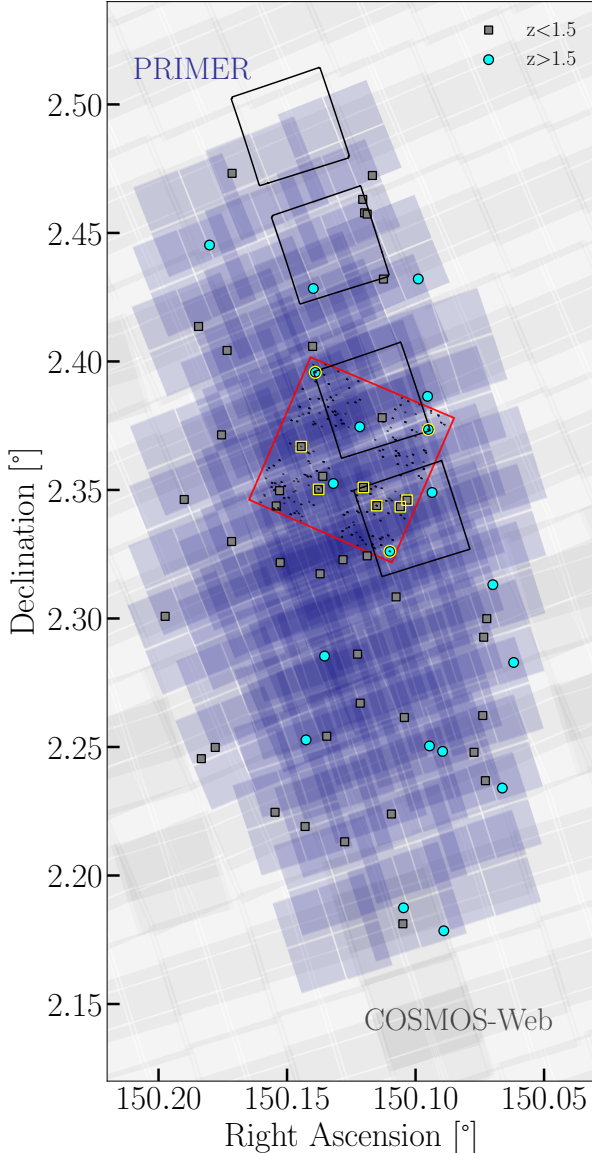


Figure 2. JWST/NIRCam observations of the COSMOS-Web and PRIMER surveys as gray- and blue-shaded areas, respectively, with roughly $\sim 0.037 \text{ deg}^2$ of overlapping area. Grey squares and cyan circles indicate the positions of transients presented in this study with redshifts of $z < 1.5$ and $z > 1.5$, respectively. Over-plotted are footprints of NIRSpec/MSA (red square) and NIRCam (black square) from follow-up observations obtained via a Director’s Discretionary Time Proposal (PID 6585; PI Coulter), described in detail in Section 5.1. NIRSpec MSA slitlets used in that program are shown with small black lines. SNe for which MSA spectra were obtained are outlined in yellow.

matters even more complicated, optimal subtractions require alignment and differencing to be performed at the exposure level before mosaics are created (e.g., C. DeCoursey et al., 2025a), necessitating complex and complicated handling of the many dithers that go into cre-

ating the final mosaic. This process entails careful management of numerous individual dithers that collectively contribute to the final integrated image, thereby motivating the development of a specialized, JWST-specific difference-imaging pipeline.

The combined sensitivity of JWST, noise characteristics of the detectors, and cosmic rays in the data yield potentially hundreds of sources that require detailed vetting in each NIRCam pointing (e.g., C. DeCoursey et al., 2025a). Filtering out real sources, as well as characterization and prioritization of high- z SNe for dedicated follow-up, is therefore a critical part of the process. In this section, we describe the detailed steps we take to identify SN candidates and apply various cuts to create our final COSMOS-Web/PRIMER SN sample, hereafter referred to as the COSMOS sample.

3.1. Image reduction and alignment

All NIRCam observations were processed using the JWST Calibration Pipeline (H. Bushouse et al., 2023), with additional modifications aimed at enhancing image quality and astrometric accuracy. We provide a brief summary here; a detailed account of the data reduction and mosaic creation is provided in M. Franco et al. (2025). The raw NIRCam exposures were sourced from the Mikulski Archive for Space Telescopes (MAST)³⁴ and processed using pipeline version 1.14.0, incorporating custom improvements, some inspired by M. B. Bagley et al. (2023). These refinements included suppression of $1/f$ noise, background subtraction, removal of artifacts such as wisps, and detection and masking of defective pixels. Calibration was carried out using the Calibration Reference Data System (CRDS) pmap-1223, corresponding to the NIRCam instrument configuration imap-0285. The final science mosaics for both COSMOS and PRIMER were generated separately with stage 3 of the JWST pipeline at resolutions of $0.^{\prime\prime}03$ per pixel for both short- (SW) and long-wavelength (LW) filters, ensuring optimal spatial detail, and also at the native $0.^{\prime\prime}06$ per pixel for accurate photometric measurements in the LW filters.

Astrometric alignment was performed using the JWST/HST Alignment Tool (JHAT; A. Rest et al. 2023), which registers the individual exposure NIRCam images (i.e., CALs) to a reference catalog constructed from pre-existing HST/ACS F814W mosaics (A. M. Koekemoer et al., 2007). The astrometry was tied to Gaia Early Data Release 3 (EDR3; Gaia Collaboration et al. 2021), yielding a median absolute positional off-

³⁴ <https://mast.stsci.edu/>

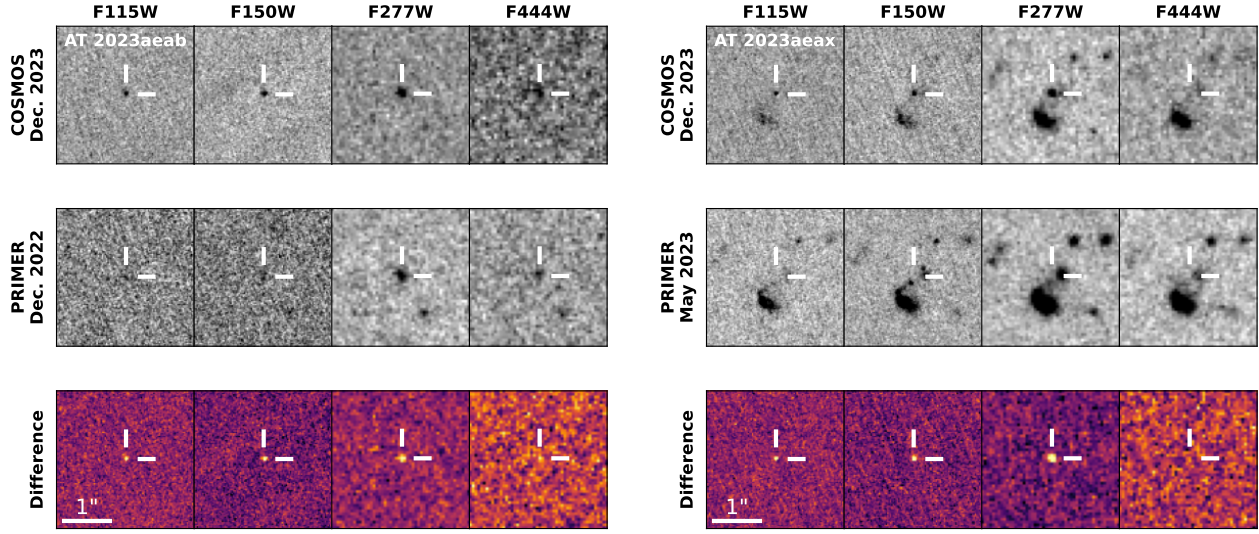


Figure 3. Cutouts for SN 2023aeab and SN 2023aeax (SN#1 and SN#4 in Table 2, respectively), both discussed throughout the text. Shown are the (*top*) discovery epoch from COSMOS-Web, (*middle*) template from PRIMER, and (*bottom*) difference image.

set of less than 5 mas and a median absolute deviation (MAD) below 12 mas across all filters.

3.2. Difference imaging

We generated difference images by subtracting the PRIMER images from the COSMOS images in each respective overlapping filter (Figure 3). We use `Hotpants` (A. Becker, 2015) to match the spatially-varying PSF kernel within a given filter between the COSMOS and PRIMER data sets, applying the general parameter setup and convolution direction described in A. Rest et al. (2014) and R. Angulo et al. (2025). For the LW, we produced two sets of difference images: one set for the transient detection with a pixel scale of $0''.03/\text{pixel}$ matching the SW pixel scale (see Section 3.3), and the other for forced photometry using a pixel scale of $0''.06/\text{pixel}$ nearly identical to the LW native pixel scale in order to avoid correlated noise (see Section 3.4).

3.3. Source detection

To identify transient candidates, source detection is easier when both the SW and LW have the same pixel scale ($0''.03/\text{pixel}$), as the pixels are identically registered across bands. For the LW, these mosaics are roughly half the native pixel scale, which is not ideal for the most accurate photometry due to the correlated noise in oversampled images (e.g., C. DeCoursey et al., 2025a). We note that for the final forced photometry,

all difference images have pixel scales close to the native pixel scale (see section 3.4). We use `Photutils` (L. Bradley et al., 2025) on the difference images of all filters to identify positive detections (P. B. Stetson, 1987; L. Bradley et al., 2024). We set the `fwlm` (full-width half-max) to ~ 2 pixels ($0''.06$) for SW images and ~ 4 pixels ($0''.12$) for resampled LW images. The `DAOStarFinder` threshold parameter is set to 3 times the background standard deviation returned from `astropy sigma_clipped_stats` with `sigma=3.0`. Following C. DeCoursey et al. (2025a), we choose not to constrain the `sharpness` parameter, as bright transients that are surrounded by subtraction artifacts in the difference images can have a wide variety of `sharpness` values, and the image border (within $3 \times \text{FWHM}$ from an edge) was excluded from the search. For all sources with signal-to-noise ratios (S/N) above 3, aperture photometry is measured using an $r=0''.1$ circular aperture with a sky annulus of $r=0''.1\text{--}0''.2$. Photometric errors are based upon the annulus sky noise combined with a Poisson uncertainty is calculated from the measured flux. Using this photometry, measured in all filters, we select transient candidates with *either* $\text{S/N} \geq 5$ in at least one band *or* $\text{S/N} \geq 3$ in at least two bands.

With these criteria, the sample of potential transients is reduced to a manageable hundreds of sources per difference image. We manually examine individual image

and difference image cutouts for all filters, as well as light curve and (apparent) host galaxy information, for all transient candidates. The most common false positives are cosmic rays, diffraction spikes, and difference image artifacts in the cores of bright, point-source-like objects.

In addition, we must consider contamination from real compact astrophysical sources, including active galactic nuclei (AGN), gamma ray burst (GRB) afterglows and tidal disruption events (TDEs). As discussed in Section 3.3 of C. DeCoursey et al. (2025a), we ruled out AGN and TDEs in most cases given their offset from the host nucleus. In a limited number of cases with nuclear variability, we have cross-matched our transient sources with previously published AGN catalogs (J. Lyu et al., 2022) and removed any AGN candidates. We also ruled out any nuclear transients where the nucleus showed variability, but did not show clear evidence of a point source appearing (or later disappearing). We have no efficient way to filter GRB afterglows, but we note the rates of GRBs are just a few percent of CCSNe (D. Guetta & M. Della Valle, 2007), so we do not consider them as significant contaminants in our sample.

All together, we identify 68 transients brightening (Table 1). While we don't perform any qualitative or quantitative tests for detection efficiency, we refer to a relevant analysis in (C. DeCoursey et al., 2025a), which performed artificial star injection tests and found roughly 80% recovery rates down to ~ 30 AB mag in the JADES transient sample. COSMOS is shallower by ~ 2 magnitudes, so we estimate a roughly 80% detection efficiency

at ~ 28 AB mag and close to 100% at brighter magnitudes in our COSMOS transient sample. The detection efficiency doesn't directly impact any of our results in this paper, but will be discussed in more detail in future papers that focus on volumetric rates.

3.4. Forced photometry

For each source detected in Section 3.3, we perform forced photometry on mosaics from each of the individual epochs with pixel scales of 30 and 60 mas for the SW and LW channel, respectively. For each candidate, we calculate the average centroid position of all detections in the difference images. At these positions, we measure forced PSF photometry using the `space_phot` (J. Pierel, 2024) package. We build a drizzled PSF using the `spike` package (A. Polzin, 2025), which takes Level 2 PSF models from `webbpsf` v. 1.2.1 (M. D. Perrin et al., 2012, 2014)³⁵ that are temporally and spatially dependent and drizzles them together using the same pipeline implementation as the data. We then implement the `space_phot` drizzled PSF fitting routine using 5×5 pixel cutouts, and fit to the observed flux in all filters. These total fluxes, which are in units of MJy/sr, are converted to AB magnitudes using the pixel scale of each image ($0''.03/\text{pix}$ for SW, $0''.06/\text{pix}$ for LW). A final source of photometric uncertainty is a systematic uncertainty on the zero-points, which is $\lesssim 0.01$ mag for all filters (M. L. Boyer et al., 2022) and negligible compared to the uncertainties derived by the `space_phot` PSF fitting algorithm. Table 1 lists the photometry for both the brightest and F150W filters, while a full table of all photometry is included in the digital supplement.

Table 1. COSMOS Classifications Data

Name	RA	DEC	z	Brightest	Brightest	F150W	BIC Ia	BIC CC
(AT)			(err)	Mag (err)	Filter	Mag (err)		
2023aebb	10:00:16.783	+02:18:47.34	5.20 (0.14)	27.80 (0.21)	F277W	—	3.50	3.02
2023aebi	10:00:21.361	+02:10:42.55	4.22 (0.14)	27.20 (0.23)	F444W	29.40 (0.75)	4.74	5.34
2023aebl	10:00:15.901	+02:14:02.46	4.02 (0.14)	26.90 (0.08)	F150W	26.90 (0.08)	9.31	13.14
2023aeab	10:00:33.363	+02:23:44.70	3.55 (0.09)	27.20 (0.09)	F115W	27.50 (0.07)	58.68	35.55
2023aeaf	10:00:22.800	+02:22:24.61	3.55 (0.12)	27.50 (0.13)	F150W	27.50 (0.13)	18.71	27.17
2023aeag	10:00:29.211	+02:22:28.53	3.51 (0.07)	26.00 (0.12)	F277W	28.10 (0.16)	53.13	162.36
2023adzt	10:00:22.456	+02:20:56.46	2.35 (0.16)	27.10 (0.06)	F150W	27.10 (0.07)	10.36	17.74
2023aeax	10:00:26.401	+02:19:33.97	2.25 (0.10)	26.00 (0.04)	F150W	26.00 (0.04)	8.30	45.57

Table 1 *continued*

³⁵ <https://webbpsf.readthedocs.io>

Table 1 (*continued*)

Name	RA	DEC	z	Brightest	Brightest	F150W	BIC Ia	BIC CC
(AT)			(err)	Mag (err)	Filter	Mag (err)		
2023aeam	10:00:34.227	+02:15:09.97	2.18 (0.11)	26.10 (0.04)	F150W	26.10 (0.04)	9.80	55.58
2023aebk	10:00:25.124	+02:11:14.74	2.14 (0.14)	27.00 (0.07)	F150W	27.00 (0.07)	7.39	9.37
2023aeal	10:00:22.698	+02:15:01.45	1.90 (0.14)	27.90 (0.22)	F150W	27.90 (0.22)	7.56	15.37
2023aeaa	10:00:22.878	+02:23:11.13	1.89 (0.14)	27.40 (0.10)	F150W	27.80 (0.15)	21.69	28.45
2023aeak	10:00:21.473	+02:14:53.80	1.88 (0.10)	25.60 (0.04)	F115W	26.10 (0.04)	8.05	29.30
2023aebf	10:00:22.782	+02:10:31.54	1.75 (0.14)	25.40 (0.11)	F277W	—	1.12	0.03
2023adzw	10:00:31.677	+02:21:09.06	1.75 (0.14)	27.30 (0.10)	F115W	27.50 (0.08)	8.88	13.67
2023adze	10:00:33.547	+02:25:42.12	1.70 (0.13)	27.00 (0.10)	F115W	27.10 (0.07)	4.40	6.85
2023adzi	10:00:23.748	+02:25:55.56	1.69 (0.13)	26.70 (0.10)	F115W	27.10 (0.07)	4.43	8.37
2023adyx	10:00:43.238	+02:26:43.05	1.64 (0.14)	27.60 (0.16)	F277W	27.70 (0.17)	2.77	24.09
2023aeaq	10:00:32.498	+02:17:07.33	1.61 (0.14)	27.30 (0.08)	F150W	27.30 (0.08)	8.03	14.68
2023adzo	10:00:39.312	+02:24:54.30	1.52 (0.15)	27.70 (0.13)	F277W	—	0.98	7.55
2023adyy	10:00:14.838	+02:16:58.39	1.52 (0.13)	26.60 (0.09)	F115W	27.10 (0.10)	4.40	6.36
2023adzq	10:00:25.420	+02:20:36.49	1.49 (0.10)	25.90 (0.04)	F115W	26.00 (0.03)	—	42.64
2023aeav	10:00:30.774	+02:19:22.36	1.48 (0.10)	27.20 (0.11)	F115W	27.70 (0.11)	7.52	11.44
2023adzy	10:00:34.676	+02:22:00.76	1.45 (0.13)	27.40 (0.14)	F150W	27.40 (0.14)	7.27	43.29
2023aeas	10:00:25.818	+02:18:30.19	1.43 (0.07)	25.90 (0.04)	F115W	25.90 (0.03)	11.85	48.17
2023adzp	10:00:43.731	+02:20:18.18	1.40 (0.13)	26.80 (0.06)	F115W	27.10 (0.07)	4.50	13.99
2023aebh	10:00:37.121	+02:13:28.53	1.39 (0.07)	25.70 (0.04)	F277W	27.70 (0.15)	88.94	440.70
2023adzn	10:00:45.601	+02:20:46.62	1.38 (0.14)	28.00 (0.20)	F150W	28.00 (0.20)	4.51	46.92
2023adzx	10:00:32.664	+02:21:19.14	1.37 (0.10)	27.00 (0.08)	F115W	27.10 (0.07)	10.75	17.34
2023aean	10:00:32.292	+02:15:15.07	1.29 (0.10)	25.70 (0.05)	F115W	26.00 (0.04)	—	10.98
2023aebe	10:00:34.317	+02:13:08.65	1.11 (0.12)	26.70 (0.12)	F115W	27.10 (0.13)	4.52	11.46
2023aeai	10:00:44.004	+02:14:43.65	1.10 (0.11)	25.20 (0.03)	F115W	25.40 (0.03)	4.46	11.31
2023aebj	10:00:25.184	+02:10:52.39	1.10 (0.14)	28.50 (0.22)	F277W	28.70 (0.34)	6.34	55.84
2023adzs	10:00:24.796	+02:20:45.70	1.09 (0.13)	26.60 (0.08)	F115W	26.80 (0.07)	17.76	21.90
2023aeac	10:00:33.613	+02:24:21.12	1.01 (0.13)	26.40 (0.11)	F115W	26.90 (0.11)	4.50	13.07
2023aebc	10:00:18.539	+02:14:52.54	1.01 (0.10)	25.80 (0.04)	F115W	26.30 (0.04)	7.86	7.95
2023aebd	10:00:30.622	+02:12:47.26	1.01 (0.12)	26.60 (0.10)	F115W	26.90 (0.09)	10.06	14.71
2023aeba	10:00:17.348	+02:17:59.73	0.93 (0.15)	27.30 (0.07)	F277W	27.40 (0.09)	38.96	118.65
2023aeap	10:00:29.165	+02:16:01.36	0.85 (0.12)	24.00 (0.02)	F115W	24.30 (0.02)	—	13.93
2023adzc	10:00:24.453	+02:25:34.08	0.70 (0.07)	25.40 (0.06)	F115W	25.90 (0.06)	158.50	162.61
2023adzj	10:00:42.116	+02:22:17.16	0.68 (0.10)	27.20 (0.17)	F115W	28.00 (0.23)	2.77	32.92
2023aeat	10:00:32.912	+02:19:02.59	0.67 (0.15)	26.70 (0.08)	F150W	26.80 (0.09)	—	726.95
2023adyz	10:00:41.132	+02:28:23.49	0.65 (0.15)	25.70 (0.04)	F115W	26.00 (0.05)	2.78	850.51
2023adzm	10:00:44.261	+02:24:48.99	0.60 (0.14)	25.10 (0.03)	F115W	25.20 (0.03)	2.77	1230.00
2023aeaw	10:00:28.512	+02:19:27.67	0.59 (0.14)	27.50 (0.26)	F150W	27.80 (0.33)	6.11	21.87
2023aebm	10:00:17.478	+02:14:12.79	0.59 (0.15)	27.90 (0.20)	F150W	27.90 (0.20)	3.36	18.52
2023aeao	10:00:25.046	+02:15:41.35	0.55 (0.15)	27.40 (0.17)	F115W	27.80 (0.16)	2.77	212.18
2023aeay	10:00:17.726	+02:15:44.07	0.55 (0.15)	26.40 (0.07)	F115W	26.60 (0.05)	2.77	932.96

Table 1 *continued*

Table 1 (*continued*)

Name	RA	DEC	z	Brightest	Brightest	F150W	BIC Ia	BIC CC
(AT)			(err)	Mag (err)	Filter	Mag (err)		
2023adzz	10:00:27.114	+02:22:41.22	0.54 (0.15)	26.70 (0.11)	F115W	27.40 (0.16)	5.95	420.23
2023aeah	10:00:47.380	+02:18:03.00	0.53 (0.15)	26.00 (0.06)	F115W	26.20 (0.05)	2.77	716.20
2023adzd	10:00:28.931	+02:27:46.92	0.49 (0.15)	25.90 (0.06)	F115W	26.30 (0.05)	—	439.38
2023aeau	10:00:36.637	+02:19:18.31	0.48 (0.14)	26.00 (0.05)	F115W	26.10 (0.03)	5.63	18826.82
2023aebg	10:00:26.253	+02:13:26.14	0.41 (0.14)	24.30 (0.02)	F115W	24.80 (0.02)	—	6507.36
2023adzr	10:00:27.624	+02:20:38.05	0.39 (0.09)	25.50 (0.01)	F150W	25.50 (0.02)	5.75	—
2023adzh	10:00:26.997	+02:25:55.38	0.30 (0.13)	26.90 (0.04)	F150W	26.90 (0.04)	2.78	8268.20
2023adzg	10:00:28.671	+02:27:23.58	0.30 (0.09)	27.30 (0.13)	F115W	—	—	33.05
2023adza	10:00:28.517	+02:27:26.43	0.30 (0.15)	26.00 (0.08)	F115W	26.40 (0.08)	2.77	10683.38
2023adzb	10:00:28.763	+02:27:28.14	0.26 (0.13)	25.60 (0.05)	F115W	26.00 (0.05)	2.77	25543.45
2023aeaz	10:00:17.636	+02:17:33.73	0.25 (0.14)	27.60 (0.10)	F150W	27.60 (0.10)	—	150.97
2023adzf	10:00:28.030	+02:28:20.46	0.17 (0.07)	27.30 (0.07)	F150W	27.30 (0.07)	22.77	230.86
2023aeear	10:00:29.417	+02:17:10.03	0.11 (0.05)	26.00 (0.03)	F115W	26.10 (0.02)	7.14	48558.67
2023adzu	10:00:33.048	+02:21:00.96	0.06 (0.04)	27.40 (0.07)	F150W	27.40 (0.07)	—	179.34
2023aeae	10:00:36.699	+02:20:58.98	0.06 (0.06)	26.40 (0.06)	F115W	27.00 (0.06)	—	2770.96
2023aead	10:00:37.010	+02:20:37.63	0.06 (0.04)	27.40 (0.08)	F150W	28.00 (0.13)	—	191.36
2023adzk	10:00:41.600	+02:24:15.36	0.03 (0.06)	27.90 (0.24)	F150W	27.90 (0.24)	24.06	8.14
2023adzl	10:00:41.177	+02:19:47.82	0.01 (0.06)	24.40 (0.01)	F150W	24.40 (0.01)	493.75	11698.89
2023adzv	10:00:28.871	+02:21:03.58	0.01 (0.06)	28.10 (0.25)	F150W	28.10 (0.25)	—	23.53
2023aeaj	10:00:42.706	+02:14:59.40	0.01 (0.06)	27.60 (0.14)	F150W	27.60 (0.14)	33.96	18.09

NOTE— Column (1): Object name (AT designation). Column (2): Right ascension (J2000). Column (3): Declination (J2000). Column (4): Host photo-redshift with uncertainty (Section 4.1). Column (5): Brightest magnitude (AB) with error. Column (6): Filter associated with brightest magnitude. Column (7): F150W magnitude with error. Column (8): BIC value for Type Ia light-curve fit. Column (9): BIC value for core-collapse light-curve fit.

4. ANALYSIS

We have identified a total of 68 SNe in the COSMOS ample (Table 1). Figure 2 shows each SN position in the COSMOS-Web/PRIMER footprint. With only one epoch of photometry (in most cases), we perform a host-galaxy assignment, host photo- z fit, photometric classification, and color-magnitude diagram evaluation. Taken together, these results provide a useful characterization of each event and enable us to select targets of interest for focused follow-up campaigns.

4.1. Host galaxies and redshifts

SN candidates are required to match a nearest-neighbor host galaxies within $4''$ of the SN because we need a host photo- z to perform our analysis. In other words, there may have been some hostless SNe that we overlooked. In a majority of cases, this technique led to one obvious host candidate. In 5% of cases, the most

likely host was more ambiguous, which led to additional visual inspection that incorporated factors such as transient color and the likely lowest redshift host (i.e., for two possible nearby hosts at equal distance from the transient, and all other things being equal, the lower redshift host as assigned). This technique differs slightly from the “directional light radius” (DLR) analysis (R. R. Gupta et al., 2016) used for the host-galaxy assignment of the JADES transient sample (C. DeCoursey et al., 2025a). We note, however, that JADES is deeper with higher spatial confusion and therefore requires that more complex approach.

The host galaxy properties are measured using an internally created catalog following the methodology of the COSMOS2025 catalog described in M. Shuntov et al. (2025). In contrast to the COSMOS2025 catalog, which is based on COSMOS imaging, our internal catalog uses the first epoch of NIRCam imaging from PRIMER to construct a detection image from 8 filters. PRIMER has the advantage of being deeper than COSMOS and

not containing any contaminating light from the SNe discovered in the COSMOS images.

Images are PSF homogenized to F444W, converted to SNR maps, and combined in a positive-truncated χ^2 image for the eight NIRCam filters. Sources are then extracted with SEP (K. Barbary, 2016), a Python wrapper for SExtractor (E. Bertin & S. Arnouts, 1996), using hot/cold methodology (M. Shuntov et al., 2025). Photometry is then performed in all NIRCam, HST/ACS, and WFC3 imaging filters using both fixed circular and Kron apertures. Uncertainties on photometry from SEP are added in quadrature with Poisson background noise estimates as a function of aperture size. Photometric redshifts are then fit to all sources using the EAzY SED-fitting tool (G. B. Brammer et al., 2008) with a combination of the default Flexible Stellar Population Synthesis templates (C. Conroy & J. E. Gunn, 2010), specifically QSF 12 v3, and bluer templates optimized for selecting less dusty galaxies in the EoR (R. L. Larson et al., 2023), which provide a number of models with variable Ly α escape fractions. Table 1 lists and Figure 4 plots the distribution redshifts for our sample.

We note that our internal PRIMER catalog is roughly a magnitude deeper than the published COSMOS2025 catalog. Another subtle point is that the COSMOS2025 catalog, based on COSMOS imaging, includes our transient candidates in its photometric measurements and thereby skews any of its resulting photometric redshift estimates. While most sources (80%) have consistent photometric redshifts between COSMOS2025 and our internal catalog, the remaining discrepancies are largely due to the greater depth of the PRIMER data and the absence of detected transients from our catalog.

4.2. Single-epoch photometric classification

Similar to the method implemented for the JADES sample in C. DeCoursey et al. (2025a), we classify each SN candidate using the STARDUST2 Bayesian light curve classification tool (S. A. Rodney et al., 2014), which is built on the underlying SNCosmo framework and was originally designed for classifying SNe using HST. STARDUST2 uses the SALT3-NIR model to represent Type Ia SNe (J. Guy et al., 2007; W. D. Kenworthy et al., 2021; J. D. R. Pierel et al., 2022) and a collection of spectrophotometric time series templates to represent CC SNe (27 Type II and 15 Type Ib/c). The CCSN templates are those developed for the SN analysis software SNANA (R. Kessler et al., 2009), derived from the SN samples of the Sloan Digital Sky Survey (J. A. Frieman et al., 2008; M. Sako et al., 2008; C. B. D’Andrea et al., 2010), Supernova Legacy Survey (P. Astier et al., 2006), and Carnegie Supernova Project

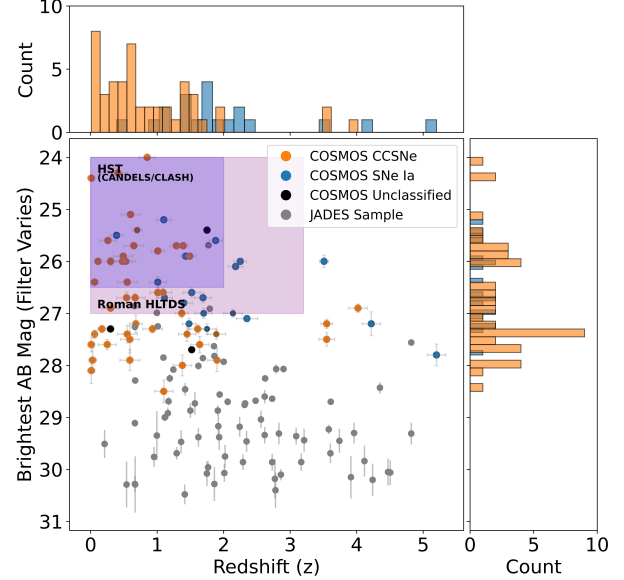


Figure 4. Magnitude and photometric redshift distribution for the COSMOS sample of SNe (Table 1), sorted by classification. Classifications assigned by STARDUST2 for targets with at least two filters in a single epoch or two epochs (but see limitations in Section 4.2). The JADES sample (C. DeCoursey et al., 2025a) is plotted for comparison (grey circles). Brightest magnitudes are chosen for plotting purposes because rest-frame photometric bands vary with redshift. However, there is no single standard rest-frame filter that we can use across all redshifts for all SNe. Shaded regions correspond to approximate sensitivity and redshift range for surveys on other telescopes, including HST CANDELS (N. A. Grogan et al., 2011; A. M. Koekemoer et al., 2011), CLASH (M. Postman et al., 2012) and Roman’s High-Latitude Time Domain Survey (HLTDS; Roman Observations Time Allocation Committee & Core Community Survey Definition Committees, 2025).

(M. Hamuy et al., 2006; M. Stritzinger et al., 2009; N. I. Morrell, 2012). The models produced for SNANA were extended to the NIR by J. D. R. Pierel et al. (2018). Within STARDUST2 a nested sampling algorithm (J. Skilling, 2004) measures likelihoods over the SN simulation parameter space, including priors on dust parameters described in S. A. Rodney et al. (2014). We use all available data for each classification, which is typically a single epoch (and sometimes more in rare cases with serendipitous observations from other programs) and up to 7 wide-band filters. STARDUST2 has been successfully implemented for single-epoch classification in the past (M. Golubchik et al., 2023; C. DeCoursey et al., 2025a), and we are able to validate it by comparing our single-epoch photometric classifications to spectroscopic classifications for existing sub-samples with spectra (see DeCoursey et al. in prep for the JADES sample and Siebert et al. in prep for this COSMOS sample).

The relative probabilities we use to determine the most-likely SN type are Bayesian probabilities from SNCosmo based upon the goodness of fit for individual SN models. They are not interpreted as the likelihood of the source being Type Ia vs. II vs. Ib/c. For example, a source may have poor fits for both Type II and Ib/c models, but the Type II model fits are comparatively better, and so the Type II probability ends up being very high despite a poor fit to the data.

Although not used directly for typing in our sample, the Bayesian Information Criterion (BIC) offers a more useful indicator of the quality of the classification. The BIC is a statistical measure used for model selection that helps choose the best-fitting model from a set of candidates. The BIC is calculated using the model's maximized log-likelihood, the number of parameters (k), and the number of data points (n). Its strength is that it balances model fit with model complexity. Models with lower BIC values are favored because they provide a better balance of explaining the data well while using fewer parameters.

Table 1 lists the BIC values for both SNe Ia and CCSN fits, but does not include the classification. Alternatively, Figure 4 includes the classifications for illustrative purposes (for targets with at least two filters in a single epoch). This is intentional because classifications, in most cases, were made with just a single epoch of data. Single epoch classifications have a number of limitations and should be treated carefully for any future rate studies. DeCoursey et al. (in prep) provide a detailed description of these limitations using the JADES sample. We stress that while we cannot consider any single classification in our sample to be correct, the relative trends and rates in 4 should be informative. A detailed discussion on the rates are beyond the scope of this paper, but will be the focus of future papers on this sample.

4.3. Color, magnitude, and redshift evaluation

Figure 4 plots the brightest magnitude (over the range of filters) for each SN against redshift for our COSMOS sample, divided by photometric classification from Section 4.2. Brightest magnitudes are chosen for plotting purposes because rest-frame photometric bands vary with redshift. The scatterplot offers a useful initial visualization of the entire distribution, particularly when comparing it against other JWST samples, such as JADES, or the capabilities of other surveys, such as HST or Roman. However, it is limited in its ability to identify targets for focused follow-up observations. The photometric classifications from Section 4.2 are only based on light-curve fits to a single epoch of photometry and have

a limited number of models that do not include tails of the CCSNe/SNe Ia distributions or extreme explosions, such as SLSNe or PISNe. Taken all together, the representation of the data in Figure 4 alone doesn't have the ability to discern potentially unique or extreme events.

A color-magnitude diagram (CMD) offers an alternative and convenient visualization of the results and can help to identify exotic SNe with extreme colors and/or luminosities, particularly when only a single epoch of data is available. By also incorporating host-galaxy redshift information, we can filter out low- z contamination events. Figure 5 plots our observational sample (black filled squares) onto a series of CMDs, each divided into redshift bins. Also included is the observational sample from JADES (grey filled circles; C. DeCoursey et al., 2025a). Contours show the theoretical color-magnitude loci for different models of SNe Ia (blue), SNe II (purple), and PISNe (red). Each SN subclass becomes redder and fainter as it evolves, which explains why each contour generally extends from the top left (bright and blue) to the bottom right (faint and red) of each plot.

The contours include models spanning a range of ages, redshifts, and reddening. The shaded tiers correspond to 68% and 95% of each distribution of theoretical models. All models are weighted equally. These contours could be loosely interpreted as 1- and 2- σ values, although note the distributions are not gaussian (see accompanying histograms) and, furthermore, the models are not weighted by likelihood. In other words, the contours do not communicate the relative frequency of occurrence of each subclass or even the models within each subclass. Histograms to the top and right of each contour provide absolute numbers to get a better set of context and relative probabilities. Note that the number of PISNe are multiplied by a factor of 100 for visualization purposes in the histogram.

5. FOLLOW-UP OBSERVATIONS

Our initial sample includes only a limited number of epochs and lacks accompanying spectra. Although a broader analysis, such as a rate study, is possible, targeted follow-up of a subsample remains important for several reasons. Detailed observations of individual high- z SNe allow us to probe the early Universe directly. These explosions provide insight into how SNe, their progenitor stars, and their host galaxies evolve with metallicity and redshift. They also offer the opportunity to identify new, extreme, or otherwise exotic events, including those arising from Population III stars or the elusive PISNe. Finally, assembling a well-sampled observational set will enable the construction of training data for machine-learning algorithms, improving our

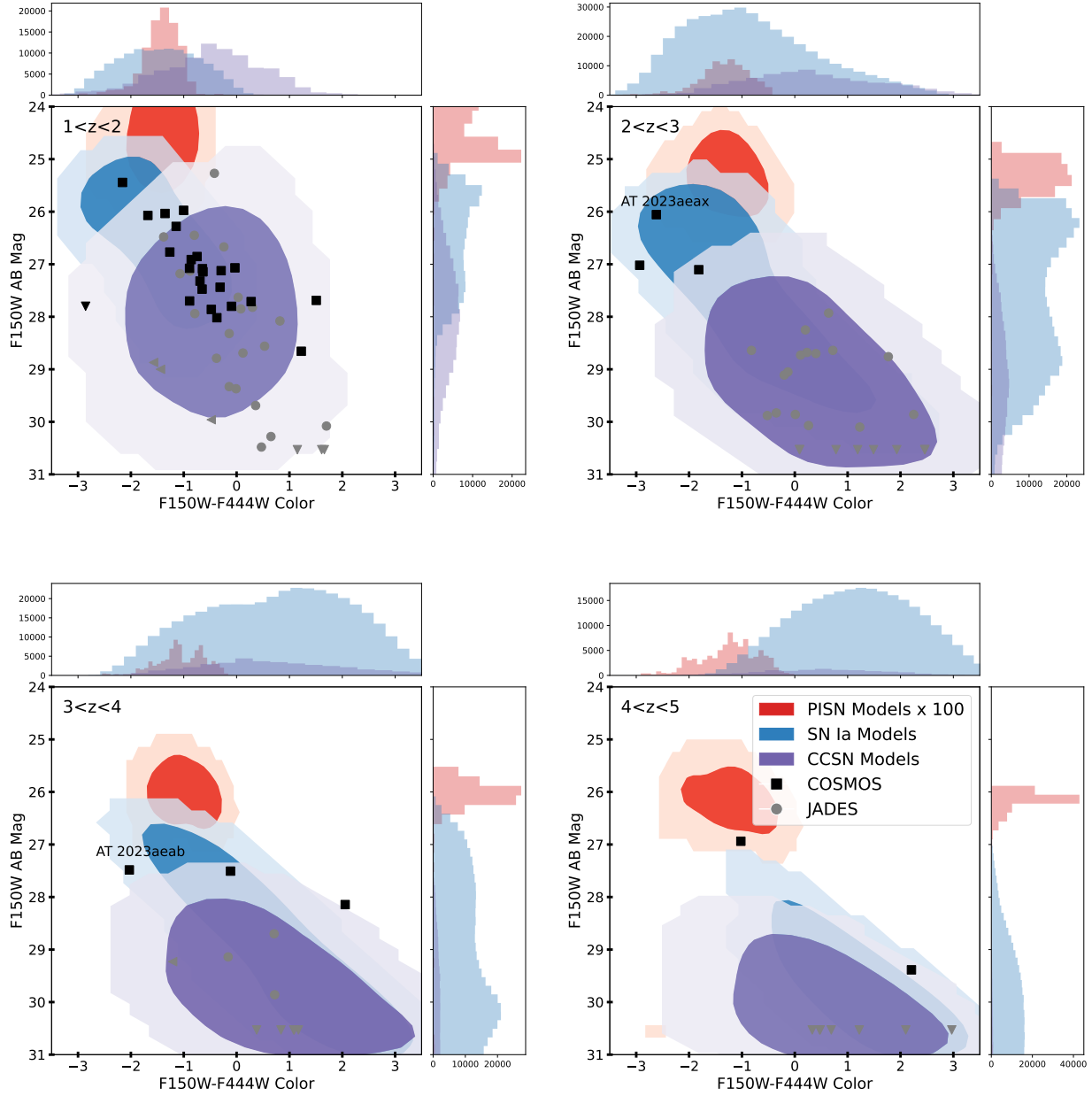


Figure 5. Color-magnitude diagram of theoretical models of SNe Ia (blue), SNe II (purple), and PISNe (red) in four redshift bins (where redshifts are photometric redshifts in Table 1). Type Ia and CCSN models are described in Section 4.2, while we use the 250 solar mass Red Supergiant (RSG) PISN models taken from D. Kasen et al. (2011). Models range in epoch and redshift, although they are limited to one observer-frame year and no extinction. The shaded tiers for each color correspond to 68% and 95% of the models for each subclass, but do not provide any information on likelihood of each model. These contours could be loosely interpreted as 1- and 2- σ values, although the distributions are not gaussian (see accompanying histograms). Overplotted are empirical results from COSMOS/PRIMER (black squares; this work) and JADES (gray circles and triangles; C. DeCoursey et al., 2025a). Histograms to the top and right of each contour provide absolute numbers. Note that the PISN histogram is multiplied by a factor of 100 for visualization purposes.

ability to filter and prioritize future candidates without requiring extensive, costly follow-up.

As previously stated, neither the COSMOS nor PRIMER programs were designed as time-domain surveys, so retiling multiple times to build light-curves is not possible. Furthermore, our sample is too large to allow individual follow-up of every source. Given the 0.037 deg^2 of overlapping area between the two surveys, any follow-up strategy therefore requires careful prioritization of the candidates and optimized observational techniques.

5.1. Candidate prioritization and identification

Figure 5 provides a visual tool for identifying SNe that are promising follow-up targets. The position of individual SNe on the CMD can quickly highlight extreme or unusual events that fall outside the typical distribution of SNe Ia and CCSNe at the corresponding redshifts (or within the typical distribution if that is the scientific goal). In the redshift bin $3 < z < 4$, one source (SN 2023aeab) stood out to us in terms of redshift, brightness, and color. Figure 6 (bottom) shows the CMD specific to SN 2023aeab’s host photometric redshift ($z \approx 3.4$; Table 1). The other COSMOS and JADES SNe from $3 < z < 4$ are also included for reference. Selecting targets of interest may vary according to an individual’s criteria. SN 2023aeab stood out to us because of its high redshift ($z \approx 3.4$), extremely blue color, and the fact that its CMD position was beyond 95% (i.e., 2σ) of the SNe II and Ia models. It is also within the 99% contour (i.e., 3σ ; not shown) of the PISN distribution. The other COSMOS targets are also potentially interesting given their positions in the CMD, but given the limited follow-up capabilities available to us, we chose SN 2023aeab as our top priority and proceeded to obtain an additional imaging epoch with NIRCam and spectroscopy with NIRSpec as part of the JWST DDT Program (PID 6585; PI Coulter).

5.2. NIRCam Imaging and NIRSpec Spectroscopy

In addition to SN 2023aeab, we designed the spectroscopy using the NIRSpec microshutter array (MSA) and optimized the NIRCam imager rotation to efficiently capture a number of other events in the field-of-view (Figure 7). SN 2023aeax, for example, is another SN that stands out given its blue color, bright magnitude, and high redshift, particularly because it falls into the typical Type Ia distribution at $z > 2$, making it an ideal candidate for follow-up (see Figures 3, 5, and 6). SN 2023aeax fits into both our MSA and NIRCam pointings.

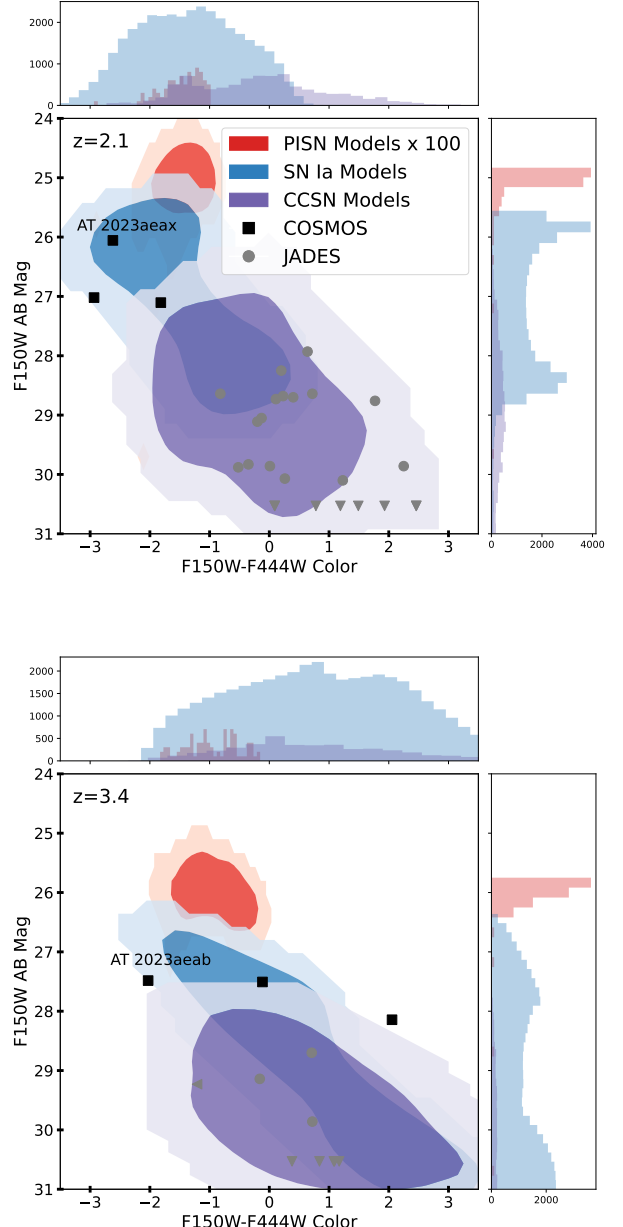


Figure 6. Same as Figure 5, but for the specific redshift of both (top) SN 2023aeax and (bottom) SN 2023aeab.

Such dynamic follow-up dramatically improves the efficiency of follow-up observations. A total of ten transients fit on our MSA pointing, with six covered by NIRSpec+NIRCam, one covered by only NIRSpec, and four covered by only NIRCam (Table 2).

We obtained NIRCam images in the filters F115W, F150W, F277W, and F444W, using the SHALLOW4 readout pattern with 8 groups and 3 standard subpixel

Table 2. Transients targeted by our followup program (PID 6585; PI Coulter)

ID	Name	Spectroscopic Redshift	Instrument
1	AT 2023aeab	3.368 (0.002)	NIRSpec+ NIRCam
2	AT 2023aeaf	3.195 (0.002)	NIRSpec+ NIRCam
3	AT 2023adzt	~2.4 (photo- z only)	NIRCam
4	AT 2023aeax	2.13 (0.01)	NIRSpec+ NIRCam
5	AT 2023adzu	1.253 (0.002)	NIRSpec+ NIRCam
6	AT 2023adzy	1.432 (0.001)	NIRSpec
7	AT 2023adzq	~ 1.5 (photo- z only)	NIRCam
9	AT 2023adzs	~ 1.1 (photo- z only)	NIRCam
10	AT 2023adzr	1.26 (0.01)	NIRSpec+ NIRCam
11	AT 2023adzv	1.857 (0.001)	NIRSpec+ NIRCam
13	AT 2023adzz	$z < 1$ (photo- z only)	NIRCam

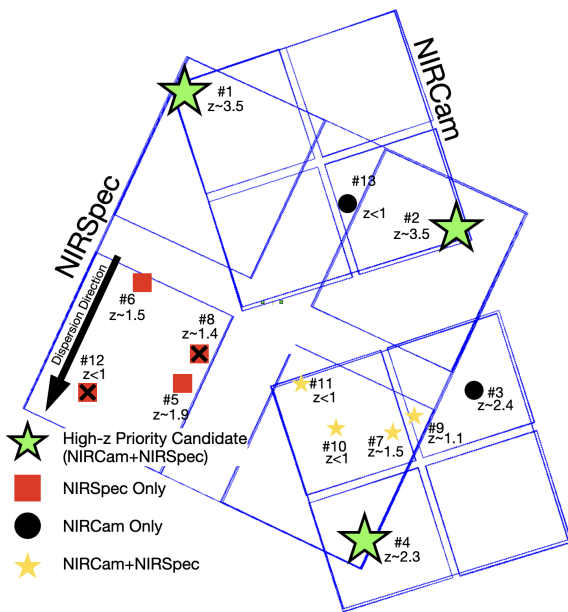


Figure 7. Design of the follow-up observations to SN 2023aeab (target #1) from the COSMOS sample (see Table 2 for target number identification). Dynamic follow-up greatly improves the efficiency, allowing us to capture multiple SNe in both our NIRCam and MSA pointings. NIRSpec targets with an ‘X’ were not observed due to overlapping spectra along the dispersion direction.

dithers, resulting into 1256 sec exposures to a depth of about 28-29 AB mag with a S/N=5. We also obtained NIRSpec MSA observations of a subsample of the transients within the NIRCam field of view, along with their hosts. Observations for both instruments were obtained on 2024 April 29 (MJD 60429).

The NIRCam imaging data were reduced and analyzed as described in Sections 3.2–3.4. The details of the MSA spectroscopic sample observations and reduction will be described in a separate paper (Siebert et al., in prep.). However, we report the spectroscopic redshifts

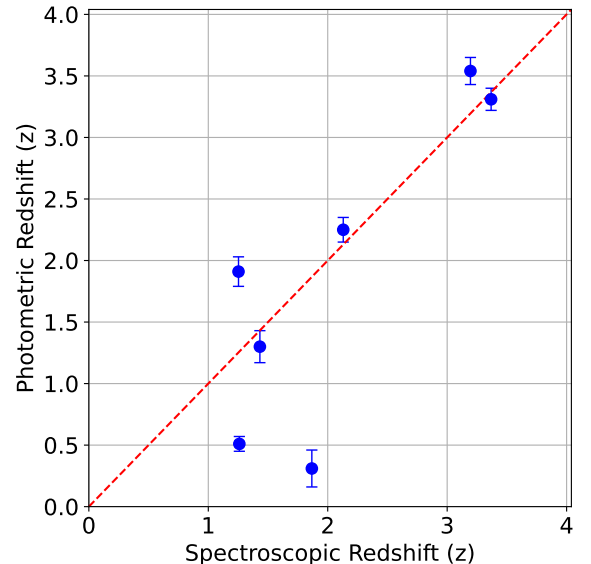


Figure 8. Plot of redshifts derived spectroscopically (Table 2) versus photometrically (Table 1).

in Table 2. For comparison, Figure 8 plots the spectroscopic versus host photometric redshifts. Qualitatively, the host photometric redshifts successfully predict the spectroscopic redshift, particularly at $z > 1$. At $z < 1$, the host photometric redshifts are less reliable, which is expected because of the lack of shorter wavelength data. The Balmer break feature is in u/b -band for low- z galaxies (J. F. Crenshaw et al., 2025). These results suggest that, assuming similar depth and wavelength coverage in future surveys, we can rely on photo- $z > 1$ to trigger for follow-up of high- z targets.

5.3. Additional Light-Curve Information

Even one additional epoch of NIRCam photometry allows us to perform more reliable light-curve fits of the

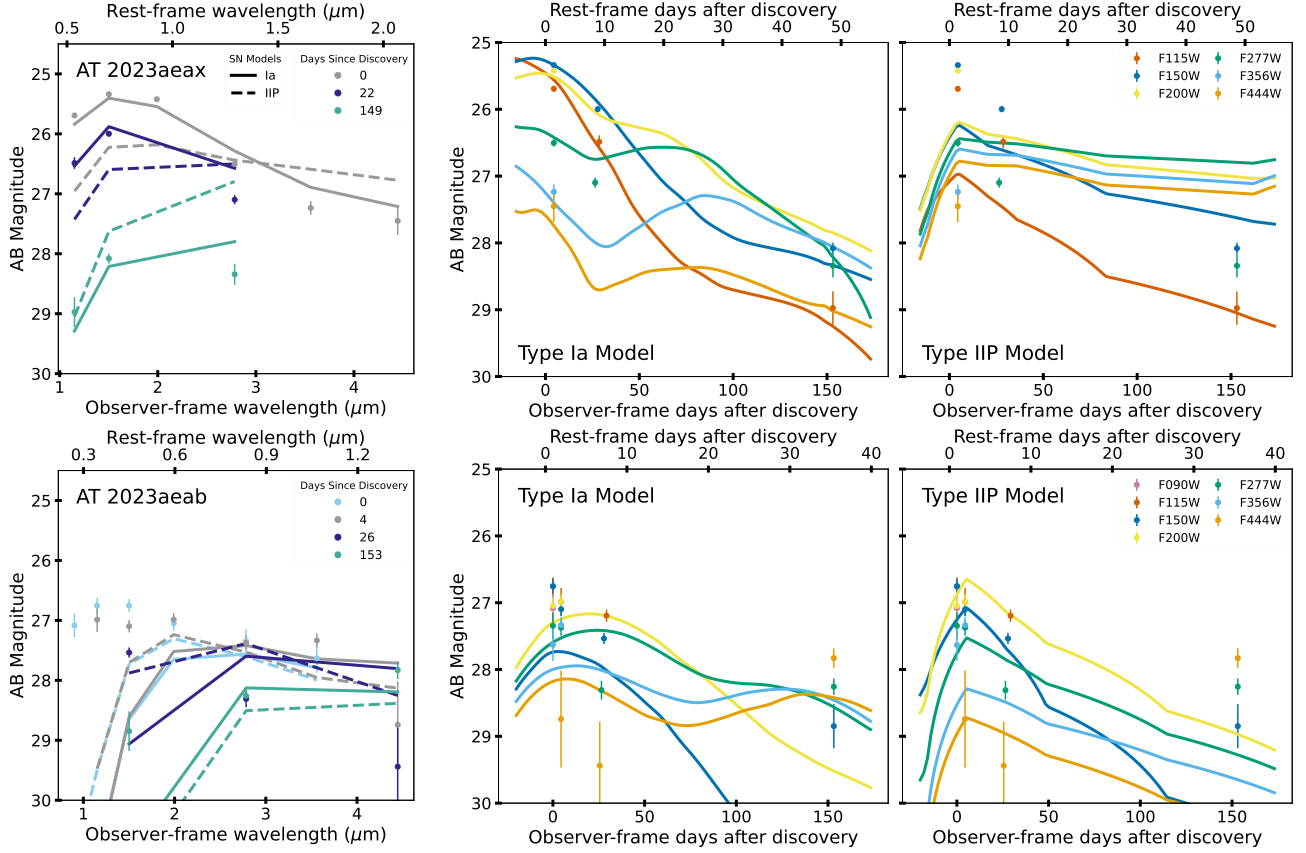


Figure 9. Photometry for (top) SN 2023aeax and (bottom) SN 2023aeab (SNe #4 and #1, respectively in Table 2). The photometry is plotted as (left) SEDs and (right) light-curves. Best-fitting generic Type Ia and CCSNe models (described in Section 4.2) are overplotted. For the SEDs, lines connect synthetic photometry calculated for each model at a particular bandpass. SN 2023aeax illustrates that Type Ia SNe and CCSNe are best differentiated with a minimum of three light-curve points over rest-frame 50 days. The early-time, short-wavelength evolution offers particularly strong leverage for disentangling the two models. For SN 2023aeab, neither SN template adequately reproduces the early-time blue emission, which suggests a more energetic, tailored SN model is needed than typically considered (Coulter et al, in prep).

SNe in our follow-up sample using similar methods as described in Section 4.2. These fits also offer a useful sanity check to our initial single epoch results.

SN 2023aeax and 2023aeab (SNe 4 and 1 in Table 2, respectively), in particular, are good test cases. SN 1 also has one additional epoch of photometry obtained serendipitously by JWST program PIDs 2514 (PI Williams). Their complete SEDs and multi-filter light-curves are plotted in Figure 9. For each light-curve, generic SNe Ia (SALT3; J. Guy et al., 2007; W. D. Kenworthy et al., 2021; J. D. R. Pierel et al., 2022) and IIP (E. Cappellaro et al., 1997; R. L. Gilliland et al., 1999; E. Baron et al., 2004) templates are overplotted for reference.

For SN 2023aeax, the combined SED and light curve are best fit by a generic Type Ia SN model, particularly at the shortest wavelengths. The brightness of the source in short wavelengths indicates that the SN was observed shortly after explosion. For SN 2023aeab, nei-

ther the generic Type Ia nor Type IIP templates provides a strong fit, although the IIP model performs better both qualitatively and quantitatively. The largest discrepancy arises at the shortest wavelengths, where SN 2023aeab also exhibits an apparent blue excess. This is consistent with the CMD in Figure 6, which places SN 2023aeab in the 95% contour ($\sim 2\sigma$) of the CCSNe distribution and approaching the PISN regime. Together, these findings reinforce the unusual nature of SN 2023aeab.

6. DISCUSSION

6.1. A New Frontier

This COSMOS sample highlights JWST’s ability to discover high- z SNe. As discussed in Section 4.2, the combined surveys, spanning ~ 133 arcmin 2 and reach depths of ~ 28 AB mag, yielded 68 SNe (~ 0.5 SN arcmin $^{-2}$) extending to $z \lesssim 5$. Although the discovery rate is lower than that of the JADES sample (> 1

SN arcmin $^{-2}$; C. DeCoursey et al., 2025a), the COSMOS sample include a larger fraction of brighter and bluer SNe (see discussion in Section 6.2). Spectroscopic follow-up observations confirm our initial classifications (Siebert et al. in prep): SN 2023aeab is a unique Type IIP at $z = 3.368$, unusually bright and blue for its class, and SN 2023aeax is a Type Ia at $z = 2.13$ caught near the peak of the light-curve. These discoveries enable us to study new physics. For example, a detailed analysis of SN 2023aeax has shown a possible redshift-dependent bias/evolution of SNe Ia at $z \gtrsim 2$ (J. D. R. Pierel et al., 2025). Future work on SN 2023aeab will examine the effects of low metallicity on Type IIP explosions in the early Universe (Coulter et al., in prep). The full sample will ultimately enable high- z SN population studies, including volumetric rates (e.g., DeCoursey et al., in prep) and links to cosmic star formation (e.g., Vassallo et al., in prep). Together, these examples illustrate only a small fraction of the high-redshift science now accessible as JWST opens this new observational frontier.

6.2. Area vs Depth

Table 3 compares the COSMOS and JADES surveys and their resulting samples. The COSMOS sample is shallower than the JADES sample by roughly two magnitudes, yet it includes events that are significantly brighter and bluer, even at comparable redshifts (Figures 5, and 6). This behavior can be understood by considering the detectability of transients such as SNe Ia and PISNe (see Figure 1). The depth of COSMOS is sufficient to detect these events near peak brightness even at high redshift, while the additional depth of JADES primarily enables detections at fainter phases of the light curve, typically at later times when the SNe are intrinsically redder, as opposed to detection of higher redshift events. As a result, increasing survey depth does not substantially increase the number of SNe Ia, CCSNe, and PISNe discovered near maximum light, nor does it preferentially yield more young, luminous events with the highest signal-to-noise. Increasing the survey area, however, directly increases the number of SNe detected near peak and enhances the probability of discovering intrinsically rare transients.

JADES reaches greater depth than COSMOS, but its smaller footprint lends itself to discoveries of transients in the central contours (i.e. 68% or 1σ) of color-magnitude space populated by typical CCSNe and SNe Ia. It is more difficult to disentangle young, unique, and/or intrinsically rare SNe in this region of the CMD. The extreme red edge of the CMD remains sparsely populated by either survey simply because PISNe are exceedingly rare, and even the larger area of the COS-

MOS sample (~ 0.037 deg 2) provides little chance for discovery. Taken together, Figures 4 and 5 illustrate that, even in the COSMOS versus JADES comparison, survey area—not depth—is the key factor for building a statistically robust SN sample at $1 < z < 3$ and for discovering the brightest, rarest events at $z > 3$.

In particular, for SNe Ia cosmology, $\sim 5 - 10$ classified, well-sampled events are required to distinguish between a luminosity bias or not at the 5σ level. For CCSN rate science, existing FUV CSFH measurements out to $z > 10$ R. J. Bouwens et al. (2023); Y. Harikane et al. (2023) indicate that > 200 classified CCSNe per year at $2 < z < 4$ are necessary to obtain $< 5\%$ precision for multiple SN subtypes. Both simulations (L.-G. Strolger et al., 2015) and empirical results (D. A. Coulter et al., 2025; C. DeCoursey et al., 2025a) show that > 0.1 deg 2 is the minimum area necessary to build such samples. For PISNe, we don't have empirical results, but models indicate 0.25 deg 2 is the minimum area to put the SLSN+PISNe rate in the single digits (T. J. Moriya et al., 2022).

6.3. Implications for future high- z surveys

These JWST discoveries from COSMOS and JADES are spectacular but represent only the tip of the iceberg because neither JADES nor COSMOS were designed for time-domain astronomy. Both data sets were plagued by a minimal number of epochs (see also DeCoursey et al. in prep) and had limited follow-up imaging and spectroscopy. Despite the COSMOS-Web/PRIMER overlap of 0.037 deg 2 area, the FOV is still too small to build the most robust statistics for both rate studies and Type Ia cosmology, not to mention achieve the necessary rates to discover the elusive PISNe. Both fields are outside JWST's Continuous Viewing Zone (CVZ), limiting year-round monitoring. A current survey, NEXUS (PID 9263; PI Shen), is located in the CVZ and designed with some SN/time-domain science in mind, but has limited utility for low redshift SN detection because of its slow cadence (~ 2 months). Its utility is also limited for high redshift SNe because of its shallow integrations and use of only two filters (F200W+F444W); high- z SN classification is difficult without F115W, which covers the bluest part of the spectrum (see the short-wavelength regime of the SED for SN 2023aeax in Figure 9). Note also that new lensing search programs with JWST templates are underway and quite promising (see PID 6882; PI Fujimoto). For example, D. A. Coulter et al. (2026) recently discovered a strongly lensed Type IIP SN at $z = 5.13$. But the strength of these observations is in the detailed follow-up of individual targets, not large samples (e.g. D. A. Coulter et al., 2026).

Table 3. Survey Details and Rates

Survey ^a	Area deg ²	Exp. Time ^a NIRCam/NIRISS (sec)	Exp. Time ^b NIRSpec (hr)	Depth ^b F277W/F356W	# CCSNe ^b $1 < z < 2$	# CCSNe ^b $2 < z < 4$	# CCSNe ^b $z > 4$
JADES	0.007	12000	7	30.0	28	33	3-7
COSMOS	0.037	1000	4	28.3	22	6	2

NOTE— ^aJADES and COSMOS taken from (C. DeCoursey et al., 2025a) and (C. M. Casey et al., 2023), respectively; ^bper epoch.

Nonetheless, the COSMOS sample lays the necessary foundation for many more studies and future work. For example, the COSMOS sample highlights the value of having a wide footprint, as it is necessary to discover the more rare and exotic phenomena. Even if a survey depth reaches only ~ 28 mag AB, this is more than sufficient to detect SNe Ia and CCSNe at $2 < z < 4$ and potentially SLSNe and PISNe out to $4 < z < 6$ (Figures 1 and 5). This sample can also be used to test the redshift evolution of properties of low- z ($z < 1$) SN samples (i.e., physics, rates, etc.), perform population studies, and conduct detailed analyses on the more unusual and rare events. Future high- z surveys will benefit from such analyses and can be optimized for specific observational goals.

A dedicated, well-designed JWST time-domain survey is needed maximize the scientific return and minimize the time spent per epoch collecting data. To achieve the science goals outlined above and properly maximize the unique phase space (primarily redshift) afforded by JWST, a properly designed survey must consider trade-offs to area, filter choice, integration times, and cadence to allow: (1) high enough number counts for statistically significant conclusions; (2) differentiation of CCSNe from SNe Ia out past cosmic noon ($z \approx 4$) for volumetric rate constraints; (3) fit a SN Ia light-curve for cosmology at redshifts higher than *Roman* (i.e., $z > 3$) ; and (4) discovery and characterization of rare SNe of interest (i.e., SLSNe and PISNe) in the low-metallicity Universe around the Epoch of Reionization (i.e., $z > 6$), where Pop III stars are most likely to exist.

Figure 1 puts some of these points into context. We model the number of SNe derived from simulations of a corresponding 5-year survey for both Type Ia SNe at redshifts $z > 3$ and Pop-III PISNe. For simplicity, the simulated surveys all have a 6-month cadence in four JWST/NIRcam bands (F115W, F150W, F277W, and F444W), all with the same limiting magnitude per epoch. The SN yields correspond to the number of SNe detected in at least one band at any phase. The red line traces the area and magnitude limits possible with 200 hours on JWST (including overheads; see Appendix A).

Increasing depth has limited benefits below about 28th magnitude, but the survey yields increase proportionally with survey area. The area and depths of several Cycle 1 JWST surveys are marked for comparison, but note these surveys are not uniform and all have different durations, filters, and cadences from the simulations. A properly designed JWST survey with an area and depth similar to the entire COSMOS-Web field (~ 28 th AB mag over ~ 0.5 deg²) would be most ideal for our desired science goals.

6.4. Synergies with *Roman*

Coordinating such a survey with the Roman High-Latitude Time-Domain Survey (HLTDS; Roman Observations Time Allocation Committee & Core Community Survey Definition Committees, 2025) offers a remarkable opportunity to combine the strengths of both surveys, maximizing JWST’s science return and enhancing HLTDS results. JWST and *Roman* could together produce an unprecedented foundation for time-domain science. Their complementary data would enable measurements of SN rates through cosmic noon, Type Ia cosmology out to $z > 2.5$, and spectroscopic confirmation of extreme SNe (SLSNe and PISNe) observed by both telescopes. JWST’s deep, long-wavelength imaging and spectroscopy of select transients will aid classification and supply a machine-learning “truth” set to identify high- z events across Roman’s wider field. We note, even for such a joint survey, the necessity for shorter wavelength photo- z ’s (Section 4.1). At $z < 5$, JWST alone cannot detect the Ly α dropout. Unlike the COSMOS field, there is not shorter wavelength data currently available in all parts of the HLTDS field. However, the HLTDS South will have *Roman*+Rubin for unimodal galaxy SEDs, while the North field is partly covered by Subaru HSC, with completion expected soon.

7. CONCLUSIONS

Two Cycle 1 treasury programs (COSMOS-Web and PRIMER) obtained overlapping images in 4 NIRCam filters (F115W, F150W, F277W, F444W). The area is > 5 times larger than JADES but not as deep (133 arcmin² to ~ 28 mag on average). A total of 68 SNe

(0.5 SNe/arcmin²) were discovered. Most of the candidates had photo- z ’s at $1 < z < 2$, but ten were at $2 < z < 5$. Compared to JADES, a smaller percentage of the sample is at higher redshifts, but the COSMOS sample tend to be brighter, bluer, and younger than the JADES sample found at comparable redshifts. This result is due to the nature of having a wide-area survey, which increases the statistical likelihood of finding not only rarer events, but also SNe at positions on the light-curve where they spend little time (i.e., near peak). This is best exemplified by SN 2023aeab (Coulter et al. in prep).

Even with a single epoch of photometry, we were able to characterize, filter, and prioritize individual SNe for detailed photometric and spectroscopic follow-up using several methods. In particular, the CMDs in Figures 5 and 6 provide a useful method for quickly visualizing the sample and identifying where individual SNe exist relative to populations of various SN subclasses. Depending on follow-up priorities, this technique offers an efficient way to identify targets of interest. Dynamic follow-up allows the NIRCam and NIRSpec orientation and slit arrangement to maximize the number of targets for follow-up in each pointing. Follow-up observations confirmed that for this limited sample, initial host photometric redshifts and classifications are reliable estimates of the actual redshift, particularly identifying intermediate and high-redshift SNe.

Certain scientific investigations are uniquely enabled by JWST. This sample provides a foundational basis for numerous follow-up studies and future investigations, while underscoring the need for a dedicated, long-term JWST SN discovery program. The results also elucidate the relative strengths and limitations of specific survey design choices—including survey area, filter selection, integration time, and cadence—thereby informing the optimization of future, dedicated JWST time-domain surveys for targeted scientific objectives.

A JWST high- z time-domain survey would also have significant synergies with the *Nancy Grace Roman Space Telescope*. Expected to launch in late 2026, *Roman* will usher in a new era of high- z discoveries, with tens of thousands of new transients to be uncovered via its pre-defined HLTDS and High-Latitude Wide-Area Survey (HLWAS; [Roman Observations Time Allocation Committee & Core Community Survey Definition Committees, 2025](#)). The sheer volume of discoveries will present a significant challenge for sorting and prioritization for detailed follow-up. While machine-learning approaches are increasingly being developed to address this problem, their performance ultimately depends on the availability of high-quality, well-characterized training data.

Smaller, but well-studied, JWST “truth” catalogs will make it possible to train and validate these tools in advance of *Roman*, enabling efficient sorting and prioritization of the most high-value high- z targets. Ultimately, follow-up photometric and spectroscopic of most of these high- z *Roman* SNe will still only be possible with JWST. A new era of time domain astronomy is upon us, and these latest JWST results are just the beginning.

AUTHOR CONTRIBUTIONS

Ori D. Fox and Armin Rest contributed equally to this work and are considered co-first authors. All authors discussed the results and commented on the manuscript.

ACKNOWLEDGMENTS

The STScI TSST group acknowledges partial support from JWST-GO-06541, JWST-GO-06585, and JWST-GO-05324. This work was made possible by utilising the CANDIDE cluster at the Institut d’Astrophysique de Paris. The cluster was funded through grants from the PNCG, CNES, DIM-ACAV, the Euclid Consortium, and the Danish National Research Foundation Cosmic Dawn Center (DNRF140). It is maintained by Stephane Roubenol. GEM acknowledges the Villum Fonden research grants 37440 and 13160. The Cosmic Dawn Center (DAWN) is funded by the Danish National Research Foundation under grant DNRF140. This project has received funding from the European Union’s Horizon 2020 research and innovation programme under the Marie Skłodowska-Curie grant agreement No 101148925. The French contingent of the COSMOS team is partly supported by the Centre National d’Etudes Spatiales (CNES). SF acknowledges support from the Dunlap Institute, funded through an endowment established by the David Dunlap family and the University of Toronto. ODF acknowledges the use of ChatGPT in helping with minor phrasing, grammar, and editing, as well as with generating some tables and figures. DBS gratefully acknowledges support from NSF Grant 2407752. MRS is supported by an STScI Postdoctoral Fellowship. JP is supported by NASA through a Einstein Fellowship grant No. HF2-51541.001 awarded by the Space Telescope Science Institute (STScI), which is operated by the Association of Universities for Research in Astronomy, Inc., for NASA, under contract NAS5-26555. Y.Z. Acknowledges support from the MAOF grant 12641898 and visitor support from the Observatories of the Carnegie Institution for Science, Pasadena, CA, where part of this work was completed. N.E.D acknowledge support from NSF grants LEAPS-2532703 and AST-2510993.

Facilities: JWST, HST

Software: astropy (Astropy Collaboration et al., 2022), EAZY and eazy-py (G. B. Brammer et al., 2008), STARDUST2 (S. A. Rodney et al., 2014), JHAT (A. Rest et al., 2023)

APPENDIX

A. SURVEY TIME DEPENDENCE ON DEPTH AND AREA

Observations with *JWST* have significant overheads due to various factors (e.g., guide star acquisition, filter change, end slew), which makes it difficult to accurately estimate the total amount of time needed to obtain 1 epoch of a mosaic to a given depth. Instead of trying to estimate each different source of overhead in detail, we empirically determine the relations between survey time, depth, and area using representative mosaics calculated with the Astronomer’s Proposal Tool (APT)³⁶.

For the purpose of this paper, we use two NIRCam exposures (i.e., 4 filters), which we consider best for transient discovery and preliminary classification with light curve fitting to guide follow-up observations. We also use 3 small dither positions, which we find to be the minimum for adequate cosmic ray rejection. Table 4 shows the NIRCam setup used for a range of possible exposure times.

For each exposure time, we calculate the total charged time t_{total} for a set of 12 mosaics with (x,y) ranging from (1,1) to (50,20), i.e. $N_{pointing} = x \times y$ ranging from 1 to 1000. We choose $x \geq y$ since there is a few percent less demand on the time if more columns than rows are used in the mosaic. For a given exposure time, we fit the straight line of t_{total} versus $N_{pointing}$

$$t_{total} = m_1(t_{exp})N_{pointing} + b_1(t_{exp}) \quad (A1)$$

The fits are shown in Figure 1 as solid red lines, and the fitted $m_1(t_{exp})$ and $b_1(t_{exp})$ in Table 5.

We then fit a straight line to $m_1(t_{exp})$ versus t_{exp}

$$m_1 = m_2 \times t_{exp} + b_2 \quad (A2)$$

and find an excellent fit (residuals << 0.1%) with $m_2 = 2.31954$ and $b_2 = 2050.5014$. We also calculate the average $\bar{b}_1 = 1635.51$. Using Equ. A1 and A2, we can then express t_{total} as

$$t_{total} = (m_2 \times t_{exp} + b_2) \times N_{pointing} + \bar{b}_1 \quad (A3)$$

These fits are shown as dashed lines in Figure 10 for a given exposure time t_{exp} . They are excellent, with residuals $\leq 1\%$ for $N_{pointing} > 2$. For $N_{pointing} \leq 2$, the residuals are at most on the order of 5%.

We can solve Equ. A3 for t_{exp} and get

$$t_{exp} = \frac{t_{total} - b_2 \times N_{pointing} - \bar{b}_1}{m_2 \times N_{pointing}} \quad (A4)$$

For Figure 1, we can loop through $N_{pointing}$, and calculate the depth m_{depth} with

$$m_{depth} = m_{0,depth} + 2.5 \log_{10} \left(\sqrt{t_{exp}/t_{0,exp}} \right) \quad (A5)$$

Here we use as empirical anchor points $m_{0,depth} = 28.3$ and $t_{0,exp} = 1000$ seconds for F227W and F356W (C. M. Casey et al., 2023).

REFERENCES

Akins, H. B., Casey, C. M., Lambrides, E., et al. 2025,

³⁶ <https://apt.stsci.edu>

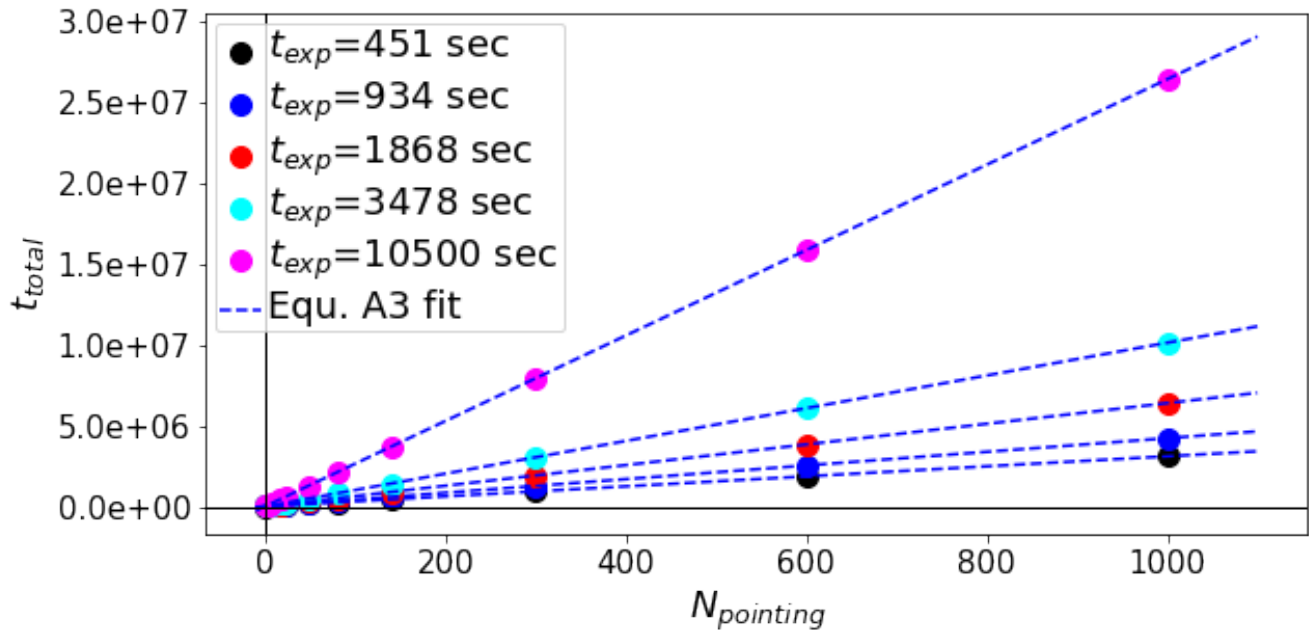
ApJ, 991, 37, doi: 10.3847/1538-4357/ade984

Table 4. NIRCam exposure setup

t_{exp} [sec]	Readout	N_{group}	N_{int}
451	SHALLOW4	3	1
934	SHALLOW4	6	1
1868	MEDIUM8	6	1
3478	DEEP8	6	1
10500	DEEP8	6	3

Table 5. Straight line fit results of t_{total} versus $N_{pointing}$

t_{exp} [sec]	m_1	b_1
451	3096.41	1636.29
934	4217.40	1635.46
1868	6381.90	1633.88
3478	10119.40	1635.63
10500	26405.41	1636.29

**Figure 10.** This figure shows the total charged time for a mosaic with $N_{pointing}$ pointings with filled circles for a given exposure time t_{exp} , calculated using the APT. The blue dashed line show the calculated t_{total} using Equ. A3

Angulo, R., Rest, A., Blair, W. P., et al. 2025, ApJS, 280, 29, doi: [10.3847/1538-4365/adf05b](https://doi.org/10.3847/1538-4365/adf05b)

Astier, P., Guy, J., Regnault, N., et al. 2006, Astronomy & Astrophysics, 447, 31, doi: [10.1051/0004-6361:20054185](https://doi.org/10.1051/0004-6361:20054185)

Astropy Collaboration, Price-Whelan, A. M., Lim, P. L., et al. 2022, ApJ, 935, 167, doi: [10.3847/1538-4357/ac7c74](https://doi.org/10.3847/1538-4357/ac7c74)

Bagley, M. B., Finkelstein, S. L., Koekemoer, A. M., et al. 2023, ApJL, 946, L12, doi: [10.3847/2041-8213/acbb08](https://doi.org/10.3847/2041-8213/acbb08)

Barbary, K. 2016, Journal of Open Source Software, 1, 58, doi: [10.21105/joss.00058](https://doi.org/10.21105/joss.00058)

Baron, E., Nugent, P. E., Branch, D., & Hauschildt, P. H. 2004, ApJL, 616, L91, doi: [10.1086/426506](https://doi.org/10.1086/426506)

Becker, A. 2015, HOTPANTS: High Order Transform of PSF ANd Template Subtraction,, Astrophysics Source Code Library, record ascl:1504.004
<http://ascl.net/1504.004>

Berman, E. M., McCleary, J. E., Koekemoer, A. M., et al. 2024, AJ, 168, 174, doi: [10.3847/1538-3881/ad6a0f](https://doi.org/10.3847/1538-3881/ad6a0f)

Bertin, E., & Arnouts, S. 1996, A&AS, 117, 393, doi: [10.1051/aas:1996164](https://doi.org/10.1051/aas:1996164)

Bouwens, R. J., Stefanon, M., Brammer, G., et al. 2023, MNRAS, 523, 1036, doi: [10.1093/mnras/stad1145](https://doi.org/10.1093/mnras/stad1145)

Boyer, M. L., Anderson, J., Gennaro, M., et al. 2022, Research Notes of the American Astronomical Society, 6, 191, doi: [10.3847/2515-5172/ac923a](https://doi.org/10.3847/2515-5172/ac923a)

Bradley, L., Sipőcz, B., Robitaille, T., et al. 2024, astropy/photutils: 1.12.0, 1.12.0 Zenodo

Bradley, L., Sipőcz, B., Robitaille, T., et al. 2025, astropy/photutils: 2.2.0, 2.2.0 Zenodo, doi: [10.5281/zenodo.14889440](https://doi.org/10.5281/zenodo.14889440)

Brammer, G. B., van Dokkum, P. G., & Coppi, P. 2008, ApJ, 686, 1503, doi: [10.1086/591786](https://doi.org/10.1086/591786)

Bushouse, H., Eisenhamer, J., Dencheva, N., et al. 2023, JWST Calibration Pipeline, 1.9.4 Zenodo, doi: [10.5281/zenodo.7577320](https://doi.org/10.5281/zenodo.7577320)

Cappellaro, E., Turatto, M., Tsvetkov, D. Y., et al. 1997, A&A, 322, 431, doi: [10.48550/arXiv.astro-ph/9611191](https://doi.org/10.48550/arXiv.astro-ph/9611191)

Casey, C. M., Kartaltepe, J. S., Drakos, N. E., et al. 2023, *ApJ*, 954, 31, doi: [10.3847/1538-4357/acc2bc](https://doi.org/10.3847/1538-4357/acc2bc)

Casey, C. M., Akins, H. B., Shuntov, M., et al. 2024, *ApJ*, 965, 98, doi: [10.3847/1538-4357/ad2075](https://doi.org/10.3847/1538-4357/ad2075)

Chen, W., Kelly, P. L., Frye, B. L., et al. 2024, *ApJ*, 970, 102, doi: [10.3847/1538-4357/ad50a5](https://doi.org/10.3847/1538-4357/ad50a5)

Conroy, C., & Gunn, J. E. 2010, FSPS: Flexible Stellar Population Synthesis, *Astrophysics Source Code Library*, record ascl:1010.043 <http://ascl.net/1010.043>

Cooke, J., Sullivan, M., Barton, E. J., et al. 2009, *Nature*, 460, 237, doi: [10.1038/nature08082](https://doi.org/10.1038/nature08082)

Cooke, J., Sullivan, M., Gal-Yam, A., et al. 2012, *Nature*, 491, 228, doi: [10.1038/nature11521](https://doi.org/10.1038/nature11521)

Coulter, D. A., Pierel, J. D. R., DeCoursey, C., et al. 2025, arXiv e-prints, arXiv:2501.05513, doi: [10.48550/arXiv.2501.05513](https://doi.org/10.48550/arXiv.2501.05513)

Coulter, D. A., Larison, C., Pierel, J. D. R., et al. 2026, arXiv e-prints, arXiv:2601.04156, doi: [10.48550/arXiv.2601.04156](https://doi.org/10.48550/arXiv.2601.04156)

Crenshaw, J. F., Leistedt, B., Graham, M. L., et al. 2025, *ApJS*, 281, 54, doi: [10.3847/1538-4365/ae14f0](https://doi.org/10.3847/1538-4365/ae14f0)

Curtin, C., Cooke, J., Moriya, T. J., et al. 2019, *ApJS*, 241, 17, doi: [10.3847/1538-4365/ab07c8](https://doi.org/10.3847/1538-4365/ab07c8)

DeCoursey, C., Egami, E., Pierel, J. D. R., et al. 2025a, *ApJ*, 979, 250, doi: [10.3847/1538-4357/ad8fab](https://doi.org/10.3847/1538-4357/ad8fab)

DeCoursey, C., Egami, E., Sun, F., et al. 2025b, arXiv e-prints, arXiv:2504.17007, doi: [10.48550/arXiv.2504.17007](https://doi.org/10.48550/arXiv.2504.17007)

Dunlop, J. S., Abraham, R. G., Ashby, M. L. N., et al. 2021, PRIMER: Public Release IMaging for Extragalactic Research,

D'Andrea, C. B., Sako, M., Dilday, B., et al. 2010, *The Astrophysical Journal*, 708, 661, doi: [10.1088/0004-637X/708/1/661](https://doi.org/10.1088/0004-637X/708/1/661)

Eisenstein, D. J., Willott, C., Alberts, S., et al. 2023, arXiv e-prints, arXiv:2306.02465, doi: [10.48550/arXiv.2306.02465](https://doi.org/10.48550/arXiv.2306.02465)

Ferrara, A., Carniani, S., Morishita, T., & Stiavelli, M. 2026, arXiv e-prints, arXiv:2601.07374. <https://arxiv.org/abs/2601.07374>

Franco, M., Casey, C. M., Koekemoer, A. M., et al. 2025, arXiv e-prints, arXiv:2506.03256, doi: [10.48550/arXiv.2506.03256](https://doi.org/10.48550/arXiv.2506.03256)

Frieman, J. A., Bassett, B., Becker, A., et al. 2008, *The Astronomical Journal*, 135, 338, doi: [10.1088/0004-6256/135/1/338](https://doi.org/10.1088/0004-6256/135/1/338)

Gaia Collaboration, Brown, A. G. A., Vallenari, A., et al. 2021, *A&A*, 649, A1, doi: [10.1051/0004-6361/202039657](https://doi.org/10.1051/0004-6361/202039657)

Gal-Yam, A. 2019, *ARA&A*, 57, 305, doi: [10.1146/annurev-astro-081817-051819](https://doi.org/10.1146/annurev-astro-081817-051819)

Gilliland, R. L., Nugent, P. E., & Phillips, M. M. 1999, *ApJ*, 521, 30, doi: [10.1086/307549](https://doi.org/10.1086/307549)

Golubchik, M., Zitrin, A., Pierel, J., et al. 2023, *MNRAS*, 522, 4718, doi: [10.1093/mnras/stad1238](https://doi.org/10.1093/mnras/stad1238)

Grogan, N. A., Kocevski, D. D., Faber, S. M., et al. 2011, *ApJS*, 197, 35, doi: [10.1088/0067-0049/197/2/35](https://doi.org/10.1088/0067-0049/197/2/35)

Guetta, D., & Della Valle, M. 2007, *ApJL*, 657, L73, doi: [10.1086/511417](https://doi.org/10.1086/511417)

Gupta, R. R., Kuhlmann, S., Kovacs, E., et al. 2016, *AJ*, 152, 154, doi: [10.3847/0004-6256/152/6/154](https://doi.org/10.3847/0004-6256/152/6/154)

Guy, J., Astier, P., Baumont, S., et al. 2007, *A&A*, 466, 11, doi: [10.1051/0004-6361:20066930](https://doi.org/10.1051/0004-6361:20066930)

Hamuy, M., Folatelli, G., Morrell, N., et al. 2006, *Publications of the Astronomical Society of the Pacific*, 118, 2, doi: [10.1086/500228](https://doi.org/10.1086/500228)

Harikane, Y., Zhang, Y., Nakajima, K., et al. 2023, *ApJ*, 959, 39, doi: [10.3847/1538-4357/ad029e](https://doi.org/10.3847/1538-4357/ad029e)

Jeon, J., Bromm, V., Venditti, A., Finkelstein, S. L., & Hsiao, T. Y.-Y. 2026, arXiv e-prints, arXiv:2601.02469, doi: [10.48550/arXiv.2601.02469](https://doi.org/10.48550/arXiv.2601.02469)

Jha, S. W., Casetti-Dinescu, D. I., Bernstein, G. M., et al. 2024, arXiv e-prints, arXiv:2405.12297, doi: [10.48550/arXiv.2405.12297](https://doi.org/10.48550/arXiv.2405.12297)

Kasen, D., Woosley, S. E., & Heger, A. 2011, *ApJ*, 734, 102, doi: [10.1088/0004-637X/734/2/102](https://doi.org/10.1088/0004-637X/734/2/102)

Kenworthy, W. D., Jones, D. O., Dai, M., et al. 2021, *ApJ*, 923, 265, doi: [10.3847/1538-4357/ac30d8](https://doi.org/10.3847/1538-4357/ac30d8)

Kessler, R., Bernstein, J. P., Cinabro, D., et al. 2009, *Publications of the Astronomical Society of the Pacific*, 121, 1028, doi: [10.1086/605984](https://doi.org/10.1086/605984)

Koekemoer, A. M., Aussel, H., Calzetti, D., et al. 2007, *ApJS*, 172, 196, doi: [10.1086/520086](https://doi.org/10.1086/520086)

Koekemoer, A. M., Faber, S. M., Ferguson, H. C., et al. 2011, *ApJS*, 197, 36, doi: [10.1088/0067-0049/197/2/36](https://doi.org/10.1088/0067-0049/197/2/36)

Larson, R. L., Hutchison, T. A., Bagley, M., et al. 2023, *ApJ*, 958, 141, doi: [10.3847/1538-4357/acfed4](https://doi.org/10.3847/1538-4357/acfed4)

Lyu, J., Alberts, S., Rieke, G. H., & Rujopakarn, W. 2022, *ApJ*, 941, 191, doi: [10.3847/1538-4357/ac9e5d](https://doi.org/10.3847/1538-4357/ac9e5d)

Moriya, T. J., Tanaka, M., Yasuda, N., et al. 2019, *ApJS*, 241, 16, doi: [10.3847/1538-4365/ab07c5](https://doi.org/10.3847/1538-4365/ab07c5)

Moriya, T. J., Inserra, C., Tanaka, M., et al. 2022, *A&A*, 666, A157, doi: [10.1051/0004-6361/202243810](https://doi.org/10.1051/0004-6361/202243810)

Moriya, T. J., Coulter, D. A., DeCoursey, C., et al. 2025, *PASJ*, 77, 851, doi: [10.1093/pasj/psaf052](https://doi.org/10.1093/pasj/psaf052)

Morrell, N. I. 2012, in IAU symposium, Vol. 279, Death of massive stars: Supernovae and gamma-ray bursts, ed. P. Roming, N. Kawai, & E. Pian, 361–362, doi: [10.1017/S174392131201335X](https://doi.org/10.1017/S174392131201335X)

Oke, J. B., & Gunn, J. E. 1983, *ApJ*, 266, 713, doi: [10.1086/160817](https://doi.org/10.1086/160817)

Perrin, M. D., Sivaramakrishnan, A., Lajoie, C.-P., et al. 2014, in Society of Photo-Optical Instrumentation Engineers (SPIE) Conference Series, Vol. 9143, Space Telescopes and Instrumentation 2014: Optical, Infrared, and Millimeter Wave, ed. J. M. Oschmann, Jr., M. Clampin, G. G. Fazio, & H. A. MacEwen, 91433X, doi: [10.1117/12.2056689](https://doi.org/10.1117/12.2056689)

Perrin, M. D., Soummer, R., Elliott, E. M., Lallo, M. D., & Sivaramakrishnan, A. 2012, in Society of Photo-Optical Instrumentation Engineers (SPIE) Conference Series, Vol. 8442, Space Telescopes and Instrumentation 2012: Optical, Infrared, and Millimeter Wave, ed. M. C. Clampin, G. G. Fazio, H. A. MacEwen, & J. M. Oschmann, Jr., 84423D, doi: [10.1117/12.925230](https://doi.org/10.1117/12.925230)

Pierel, J. 2024, Space-Phot: Simple Python-Based Photometry for Space Telescopes, Zenodo, doi: [10.5281/zenodo.12100100](https://doi.org/10.5281/zenodo.12100100)

Pierel, J. D. R., Rodney, S., Avelino, A., et al. 2018, Publications of the Astronomical Society of the Pacific, 130, 114504, doi: [10.1088/1538-3873/aadb7a](https://doi.org/10.1088/1538-3873/aadb7a)

Pierel, J. D. R., Jones, D. O., Kenworthy, W. D., et al. 2022, ApJ, 939, 11, doi: [10.3847/1538-4357/ac93f9](https://doi.org/10.3847/1538-4357/ac93f9)

Pierel, J. D. R., Engesser, M., Coulter, D. A., et al. 2024, ApJL, 971, L32, doi: [10.3847/2041-8213/ad6908](https://doi.org/10.3847/2041-8213/ad6908)

Pierel, J. D. R., Coulter, D. A., Siebert, M. R., et al. 2025, ApJL, 981, L9, doi: [10.3847/2041-8213/adb1d9](https://doi.org/10.3847/2041-8213/adb1d9)

Polzin, A. 2025, The Journal of Open Source Software, 10, 8200, doi: [10.21105/joss.08200](https://doi.org/10.21105/joss.08200)

Postman, M., Coe, D., Benítez, N., et al. 2012, ApJS, 199, 25, doi: [10.1088/0067-0049/199/2/25](https://doi.org/10.1088/0067-0049/199/2/25)

Rest, A., Pierel, J., Correnti, M., et al. 2023, arminrest/jhat: The JWST HST Alignment Tool (JHAT), v2 Zenodo, doi: [10.5281/zenodo.7892935](https://doi.org/10.5281/zenodo.7892935)

Rest, A., Pierel, J., Correnti, M., et al. 2023, arminrest/jhat: The JWST HST Alignment Tool (JHAT), Zenodo, doi: [10.5281/zenodo.7892935](https://doi.org/10.5281/zenodo.7892935)

Rest, A., Scolnic, D., Foley, R. J., et al. 2014, ApJ, 795, 44, doi: [10.1088/0004-637X/795/1/44](https://doi.org/10.1088/0004-637X/795/1/44)

Rodney, S. A., Riess, A. G., Strolger, L.-G., et al. 2014, AJ, 148, 13, doi: [10.1088/0004-6256/148/1/13](https://doi.org/10.1088/0004-6256/148/1/13)

Roman Observations Time Allocation Committee, & Core Community Survey Definition Committees. 2025, arXiv e-prints, arXiv:2505.10574, doi: [10.48550/arXiv.2505.10574](https://doi.org/10.48550/arXiv.2505.10574)

Sako, M., Bassett, B., Becker, A., et al. 2008, The Astronomical Journal, 135, 348, doi: [10.1088/0004-6256/135/1/348](https://doi.org/10.1088/0004-6256/135/1/348)

Scoville, N., Aussel, H., Brusa, M., et al. 2007, ApJS, 172, 1, doi: [10.1086/516585](https://doi.org/10.1086/516585)

Shuntov, M., Akins, H. B., Paquereau, L., et al. 2025, arXiv e-prints, arXiv:2506.03243, doi: [10.48550/arXiv.2506.03243](https://doi.org/10.48550/arXiv.2506.03243)

Siebert, M. R., DeCoursey, C., Coulter, D. A., et al. 2024, ApJL, 972, L13, doi: [10.3847/2041-8213/ad6c32](https://doi.org/10.3847/2041-8213/ad6c32)

Skilling, J. 2004, in American institute of physics conference series, Vol. 735, American institute of physics conference series, ed. R. Fischer, R. Preuss, & U. V. Toussaint, 395–405, doi: [10.1063/1.1835238](https://doi.org/10.1063/1.1835238)

Smith, M., Sullivan, M., Nichol, R. C., et al. 2018, ApJ, 854, 37, doi: [10.3847/1538-4357/aaa126](https://doi.org/10.3847/1538-4357/aaa126)

Stetson, P. B. 1987, PASP, 99, 191

Stritzinger, M., Mazzali, P., Phillips, M. M., et al. 2009, The Astrophysical Journal, 696, 713, doi: [10.1088/0004-637X/696/1/713](https://doi.org/10.1088/0004-637X/696/1/713)

Strolger, L.-G., Dahlen, T., Rodney, S. A., et al. 2015, ApJ, 813, 93, doi: [10.1088/0004-637X/813/2/93](https://doi.org/10.1088/0004-637X/813/2/93)

Yan, H., Ma, Z., Sun, B., et al. 2023, ApJS, 269, 43, doi: [10.3847/1538-4365/ad0298](https://doi.org/10.3847/1538-4365/ad0298)